Calcium bridging drives polysaccharide co-adsorption to a proxy sea surface microlayer

*Kimberly A. Carter-Fenk,[a] Abigail C. Dommer,[b] Michelle E. Fiamingo,[a] Jeongin Kim,[a] Rommie E. Amaro,[b] and Heather C. Allen[a]**

a. Department of Chemistry and Biochemistry, The Ohio State University, Columbus, OH 43210, USA

b. Department of Chemistry and Biochemistry, University of California, San Diego, La Jolla, CA 92093, USA

Corresponding Author

* Heather C. Allen (allen@chemistry.ohio-state.edu)

Abstract

Saccharides comprise a significant mass fraction of organic carbon in sea spray aerosol (SSA), but the mechanisms through which saccharides are transferred from seawater to the ocean surface and eventually into SSA are unclear. It is hypothesized that saccharides cooperatively adsorb to other insoluble organic matter at the air/sea interface, known as the sea surface microlayer (SSML). Using a combination of surface-sensitive infrared reflection-absorption spectroscopy and all-atom molecular dynamics simulations, we demonstrate that the marine-relevant, anionic polysaccharide alginate co-adsorbs to an insoluble palmitic acid monolayer via divalent cationic bridging interactions. Ca^{2+} induces the greatest extent of alginate co-adsorption to the monolayer, evidenced by the ~30% increase in surface coverage, whereas Mg^{2+} only facilitates one-third the extent of co-adsorption at seawater-relevant cation concentrations due to its strong hydration propensity. Na^{+} cations alone do not facilitate alginate co-adsorption, and palmitic acid protonation hinders the formation of divalent cationic bridges between the palmitate and alginate carboxylate moieties. Alginate co-adsorption is largely confined to the interfacial region beneath the monolayer headgroups, so surface pressure, and thus monolayer surface coverage, only changes the amount of alginate co-adsorption by less than 5%. Our results provide physical and molecular characterization of a potentially significant polysaccharide enrichment mechanism within the SSML.

Introduction

Saccharides constitute one of the most abundant classes of organic carbon in sea spray aerosol (SSA);[1–3] but the mechanisms through which these compounds are selectively transferred from bulk seawater to the ocean surface, known as the sea surface microlayer (SSML), and finally to SSA, are not fully understood.[4] Compared to the concentration in seawater, saccharides are enriched 1.2–12.1-fold in the SSML,[5–7] 38–3700-fold in super-micron SSA,[8] and 100–930,000-fold in sub-micron SSA.[8,9] Saccharides can be covalently bound to larger, more surface-active biomolecules, such as glycoproteins or lipopolysaccharides, which adsorb to the SSML and are eventually transferred into SSA via bubble bursting at the ocean surface.[10,11] Alternatively, soluble saccharides can become enriched in SSA by forming a cooperatively adsorbed layer to insoluble organic films at the SSML primarily through electrostatic interactions.[10,12–15] Chemical composition is a significant driver of SSA particle radiative properties, so climate models require predictive representations of marine aerosol composition to accurately model climate processes in the marine boundary layer.[12,16–19] SSA containing polysaccharides, especially polysaccharides within marine microgels, comprise a significant fraction of cloud condensation nuclei (CCN)[20–23] and ice nucleating particles (INPs),[24–31] thereby affecting cloud formation and albedo. Current climate models underestimate the proportion of polysaccharides in marine aerosol.[12,16,32,33] Thus, characterization of polysaccharide enrichment mechanisms in SSA is imperative for improving aerosol representation in global climate models.

A divalent cation mediated cooperative adsorption (co-adsorption) mechanism was postulated by Schill *et al.* to explain enrichment of the monosaccharide glucuronic acid in laboratory-generated SSA.[10] Glucuronic acid likely co-adsorbs to an insoluble palmitic acid (hexadecanoic acid, $CH_3(CH_2)_{14}COOH$) monolayer via seawater divalent cationic bridging

interactions. Palmitic acid is one of the most abundant lipids in the SSML[34,35] and in nascent SSA,[34,36,37] making it a good model for insoluble organic matter in an SSML proxy film.[38–41] Co-adsorption to insoluble lipid monolayers has been indirectly observed for other saccharides and polysaccharides as well.[12–14,42] Electrostatic interactions between charged saccharides and either charged or zwitterionic lipid headgroups have been the predominant mechanism of co-adsorption proposed. For example, the cationic polysaccharide chitosan primarily interacts with negatively charged and zwitterionic phospholipids through electrostatic interactions between the chitosan ammonium and phospholipid phosphate moieties.[43–48] Chitosan co-adsorption expands the monolayer,[49] and chitosan likely intercalates into the monolayer at low mean molecular area through dispersive interactions.[47,48] Divalent cationic bridging between the anionic polysaccharide dextran sulfate and the zwitterionic phospholipids 1,2-dipalmitoyl-phosphatidylethanolamine (DPPE) and 1,2-dimyristoyl-sn-glycero-3-phosphocholine (DMPC) has also been measured.[50–52] Ca^{2+} bridges the sulfate and phosphate moieties, whereas Na^{+} does not.[51] Strength of dextran sulfate co-adsorption increases with the number of calcium bridges formed, and unlike chitosan, dextran sulfate does not intercalate into the monolayer; instead, the authors argued that strong bridging interactions tether the polysaccharide to the underside of the phosphate headgroups.[52] Thus, divalent cationic bridging interactions could promote polysaccharide co-adsorption to the SSML and enrichment in SSA.

Recent work by Hasenecz e*t al.* has shown that the polysaccharide alginate is enriched in laboratory-generated marine aerosol, and alginate enrichment can be enhanced upon adding protein and additional $CaCl_2$ salt to the model seawater solution.[53] Alginate is a type of exopolymeric substance derived from marine brown algae and bacteria;[54,55] it is composed of (1→4)-linked α-L-guluronic (G) and β-D-mannuronic (M) monomers that form a block copolymer

with random sequences of M-, G-, and MG-blocks.[56–61] Alginate polymers undergo ionic cross-linking to form hydrophilic gels via metal ion coordination primarily to the G residue carboxylic acid moieties.[58,61,62] The rigidity and stability of the hydrogels are largely driven by the M/G residue ratio and the molecular weight of the polymers,[61,63,64] but the ionic cross-linker identities and concentrations also play a crucial role.[65–70] Multivalent cations readily induce gelation, and the cation hydration free energies dictate the local interaction configurations with G residues.[70] Of the abundant seawater cations, Ca^{2+} is the most efficient gelling agent.[65,66,70] Mg^{2+} only induces gelation at high alginate concentrations (> 3 wt% alginate and $[Mg^{2+}] > 50$ mM) because of its high affinity for water such that the G residue carboxylate moieties cannot readily dehydrate Mg^{2+} for coordination.[67–70] Extensive experimental and computational studies[71–76] have investigated polysaccharide aggregation into surface-active marine gels via ionic coordination, but less is known about polysaccharide complexation to other surface-active organic molecules derived from marine biota. Enhanced saccharide enrichment in laboratory-generated SSA in the presence of divalent cations and other surface-active organic material strongly suggests a co-adsorption mechanism mediated by divalent cationic bridging.[10,53]

In this study, we examine the cationic bridging mechanism responsible for alginate co-adsorption to a deprotonated palmitic acid monolayer using surface-sensitive infrared reflection-absorption spectroscopy (IRRAS) and molecular dynamics simulations. We directly observe polyelectrolyte adsorption to an insoluble monolayer of the same charge state bridged by an ion of opposite charge. Ca^{2+} induces the greatest degree of alginate co-adsorption to the monolayer, but the divalent cationic bridges break apart upon palmitic acid protonation. Mg^{2+} also promotes co-adsorption to the deprotonated monolayer, but the interaction is much weaker due to the strong hydration of Mg^{2+}. Na^{+} alone does not facilitate alginate co-adsorption. Our detailed experimental

and computational analyses of the alginate co-adsorption mechanism to an SSML proxy film suggest that the Ca^{2+} bridge to surface-active marine organic matter is an important driver of polysaccharide enrichment in the SSML, and thus, in SSA.

Experimental and computational methods

Materials

Calcium chloride dihydrate (Certified ACS, Fisher Chemical), magnesium chloride hexahydrate (Crystalline/Certified ACS, Fisher Chemical), d_{31}-palmitic acid (98%, Cambridge Isotope Laboratories, Inc.), and d_{33}-cetyl alcohol (d_{33}-hexadecanol, 98%, Cambridge Isotope Laboratories, Inc.) were used as received. Sodium chloride (99.5%, for biochemistry, ACROS Organics™) was baked for at least 10 hours in a furnace at 650° C to remove residual organic impurities.[77] Alginic acid (sodium salt, ACROS Organics™, Lot: A0406891) was also used as received from the same batch to maximize homogeneity in molecular weight and composition. All aqueous solutions were prepared with ultrapure water (18.2 MΩ·cm, Milli-Q Advantage A10, EMD Millipore) in glassware cleaned in a piranha acid bath. Acidification by atmospheric CO_2 causes the ultrapure water pH to be 5.8 ± 0.1; hence, the pH 5.8 aqueous solutions were not pH adjusted. Atmospheric CO_2 acidifies the solutions at seawater pH too, so the solutions were initially pH adjusted to 8.6 ± 0.1 to ensure that the pH would be 8.2 ± 0.1 throughout spectral acquisition. The solution pH was increased by adding microliter aliquots of 0.33 M NaOH solution created from dissolution of sodium hydroxide pellets (98%, extra pure, ACROS Organics™) into ultrapure water, and the aqueous subphase solution pH was measured in triplicate prior to use in experiments to ensure reproducibility. Lipids were dissolved in chloroform (Reagent ACS,

99.8+%, ACROS Organics™) to prepare ~1.25 mM solutions for spreading onto the aqueous surface.

Surface pressure-area isotherms

Surface pressure – area isotherms were performed using the Wilhelmy plate method in a Teflon Langmuir trough with Delrin barriers (Biolin Scientific). The platinum Wilhelmy plate, trough, and barriers were cleaned thoroughly with ultrapure water and ethanol, and the Wilhelmy plate was fired with a Bunsen burner until red hot. Surface cleanliness of the aqueous solution was assessed by sweeping the barriers at maximum compression speed (270 mm/min/barrier) to ensure that the surface pressure did not rise above 0.20 mN/m. d_{31}-Palmitic acid dissolved in chloroform was spread dropwise onto the aqueous surface using a glass syringe (Hamilton), and the chloroform solvent was allowed to evaporate over 10 minutes. The barriers were symmetrically compressed at a rate of 5 mm/min/barrier, and constant surface pressure was maintained during spectroscopic measurements via slow barrier position fluctuations (1 mm/min/barrier).

Infrared reflection-absorption spectroscopy

Infrared-reflection absorption spectroscopy was conducted using an in-lab-built optical setup. Two planar gold mirrors positioned at 48° relative to surface normal were placed inside a Fourier transform infrared spectrometer (Spectrum 100, PerkinElmer) to direct the incident beam towards the aqueous surface and to direct the reflected light towards the liquid nitrogen-cooled HgCdTe (MCT) detector. Spectra were collected with unpolarized light as an average of 400 scans in the single-beam mode, and the spectral resolution was set to 4 cm^{-1}. Energy values were recorded between 450 and 4000 cm^{-1} in 0.5 cm^{-1} increments. Experiments were repeated in at least triplicate, and each spectrum was reported as the average of all trials. Spectral background subtraction and peak integration were performed using OriginPro 9.0. The OH stretching region

was analyzed by fitting a line between endpoints 2985 and 3800 cm^{-1} for baseline subtraction, and the area under the curve was integrated between these endpoints. The IRRAS spectra and integrated peak areas were numerically corrected to account for differences in monolayer mean molecular area (MMA) between experiments. The average MMA value of the solution containing alginate was divided by the corresponding average MMA value of the salt water solution. This ratio was then multiplied into the reflectance-absorbance values of the spectra containing alginate. Similar spectral analyses were performed in the COOH stretching (1150-1850 cm^{-1}) and CD_2 scissoring mode (1070-1110 cm^{-1}) regions, and descriptions of the peak fitting procedures can be found in the Electronic Supplementary Information (ESI). All spectra and data points represent averages of at least three measurements, and error bars represent one standard deviation from the mean.

Computational methods

Explicit solvent all-atom molecular dynamics simulations were performed using NAMD[78] at a temperature of 298.15 K. The initial configurations of each system were constructed using Packmol.[79] To approximate a TC palmitic acid monolayer at pH 5.6, palmitic acid molecules were packed into two planar 25 Å x 25 Å monolayer slabs, each containing 96 molecules. A pH of 8.2 was approximated by packing 46 molecules each of palmitate and palmitic acid into monolayer slabs of the same dimensions. The monolayer slabs were then separated on one side by vacuum and the other side with a 60 Å-deep water box with 15 proxy alginate molecules (ESI Fig. S1). The initial structure for the alginate was constructed using the CHARMM-GUI glycan modeler[80–83] and consists of 6 (1→4)-β-linked M monomers. For each representative pH, the aqueous phase either contained 0.47 M NaCl + 10 mM $CaCl_2$ or 0.47 M NaCl only. TIP3P water[84] was used in conjunction with the CHARMM36 forcefield. To improve the accuracy of sodium and calcium

interactions with the carboxylates in the monolayer and alginate, the version of CHARMM36 with an NBFIX correction (July 2018) was applied.[85–88] Production simulations consisting of 200-ns trajectories each were then performed in triplicate for a total of 600 ns per system. The production run simulation length of 200 ns was chosen to allow for any long timescale diffusion and settling of ions and alginate. Additional details and discussion about the simulation set-up and parameters are given in the ESI.

Analyses of the MD trajectories were performed in a Jupyter Notebook iPython environment. The density and radial distribution function (RDF) calculations were performed with pytraj.[89,90] Lipid order parameters were calculated using the GROMACS *gmx order* tool from GROMACS version 2018.3.[91]

Results and discussion

The mechanism of alginate co-adsorption to a d_{31}-palmitic acid ($CD_3(CD_2)_{14}COOH$) monolayer was investigated experimentally as a function of solution ionic composition, d_{31}-palmitic acid protonation state, and surface pressure. We will use the terms "monolayer" to refer to the monomolecular layer of d_{31}-palmitic acid alone and "film" to describe alginate complexed to the d_{31}-palmitic acid monolayer. Deuterated palmitic acid was used to spectrally isolate the CD_2 scissoring mode from the carboxylate stretching region. The ionic composition was selected to model concentrations of the most abundant cations in seawater: 0.47 M NaCl, 10 mM $CaCl_2$, and 53 mM $MgCl_2$.[92,93] As a direct comparison to the 10 mM $CaCl_2$ solution, alginate co-adsorption in 10 mM $MgCl_2$ aqueous solution was also measured. All aqueous solutions have a background of 0.47 M NaCl to maintain high ionic strength as in seawater.

The carboxylic acid protonation state was varied through the solution pH values of 8.2 and 5.8. Palmitic acid has a reported surface pK_a between 8.34 and 8.7,[39,94–96] and the pK_a values of alginate G and M residues are 3.7 and 3.4, respectively.[97] Thus at pH 8.2, the pH of seawater,[98] palmitic acid is partially deprotonated and alginate is fully deprotonated. At pH 5.8, palmitic acid is mostly protonated, and alginate carboxylate groups remain deprotonated. Salts can deprotonate carboxylic acids at pH values significantly below the pK_a,[40,99,100] however, so a d_{33}-cetyl alcohol (d_{33}-hexadecanol, $CH_3(CH_2)_{15}OH$) monolayer was used as a control to study alginate co-adsorption to a fully protonated monolayer. Alginic acid is insoluble in water, so a lower pH value was not tested instead to avoid significant changes in solubility. Alginate hydrolysis kinetics are also enhanced in acidic solution, thereby changing the alginate molecular weight distribution in solution over time.[101,102] Deprotonated palmitate molecules are slightly more soluble in water,[39,40] so IRRAS spectra were maintained and collected at constant surface pressure to minimize any interpretation impacts from dissolution. The surface pressure values of 5 mN/m and 25 mN/m were chosen to represent the tilted condensed (TC) and untilted condensed (UC) two-dimensional monolayer phases, respectively.[103] Both phases exhibit long-range lateral order in the alkyl tails, but the d_{31}-palmitic acid molecules in the UC phase are closer together on average (more tightly packed) and less tilted relative to surface normal.[104]

To experimentally measure co-adsorption of alginate to the d_{31}-palmitic acid monolayer, IRRAS spectra were analyzed in the OH-stretching region (2985-3800 cm^{-1}), the COOH stretching region (1150-1850 cm^{-1}), and the CD_2 scissoring mode region (1070-1110 cm^{-1}). IRRAS spectra are plotted as reflectance-absorbance (RA),

$$\mathrm{RA} = -\log\frac{R_\mathrm{f}}{R_0}, \tag{1}$$

where R_f corresponds to the film reflectance and R_0 corresponds to the reflectance of the bare aqueous solution. Hence, the signal from the interfacial film is captured, whereas the signal from the bulk aqueous phase is subtracted. When the film reflectance is greater than the solution reflectance ($R_f/R_0 > 1$), the reflectance-absorbance values are negative. Conversely, if the reflected signal from the solution is greater than that of the film ($R_f/R_0 < 1$), then the reflectance-absorbance values are positive. To isolate the signal from alginate co-adsorption due to the presence of the d_{31}-palmitic acid monolayer, alginate was also included in the aqueous solution spectrum (R_0). Yet, the contribution of alginate adsorbed to the air-water interface due to surface activity alone is small and below our spectroscopic limit of detection.

Experimental evidence of cation-specific alginate co-adsorption mechanisms

The OH stretching region provides sensitive detection of the aqueous solution reflectance, making the spectra useful for quantifying changes in interfacial coverage as a function of alginate co-adsorption. If there is no alginate co-adsorption, then the film spectrum with alginate in the solution directly overlaps the monolayer spectrum without alginate. As shown in Figs. 1a and 1c, the IRRAS OH-stretching modes are positive in sign, indicating that the OH region reflectance decreases upon spreading d_{31}-palmitic acid onto the aqueous solution. The magnitude of the reflectance-absorbance signal intensity also increases with compression of the monolayer to higher surface pressure. Thus, increasing organic surface coverage decreases reflectance from the underlying aqueous solution. Consequently, alginate co-adsorption to d_{31}-palmitic acid molecules increases surface coverage, and the OH stretching region reflectance-absorbance values increase with alginate co-adsorption to the film.

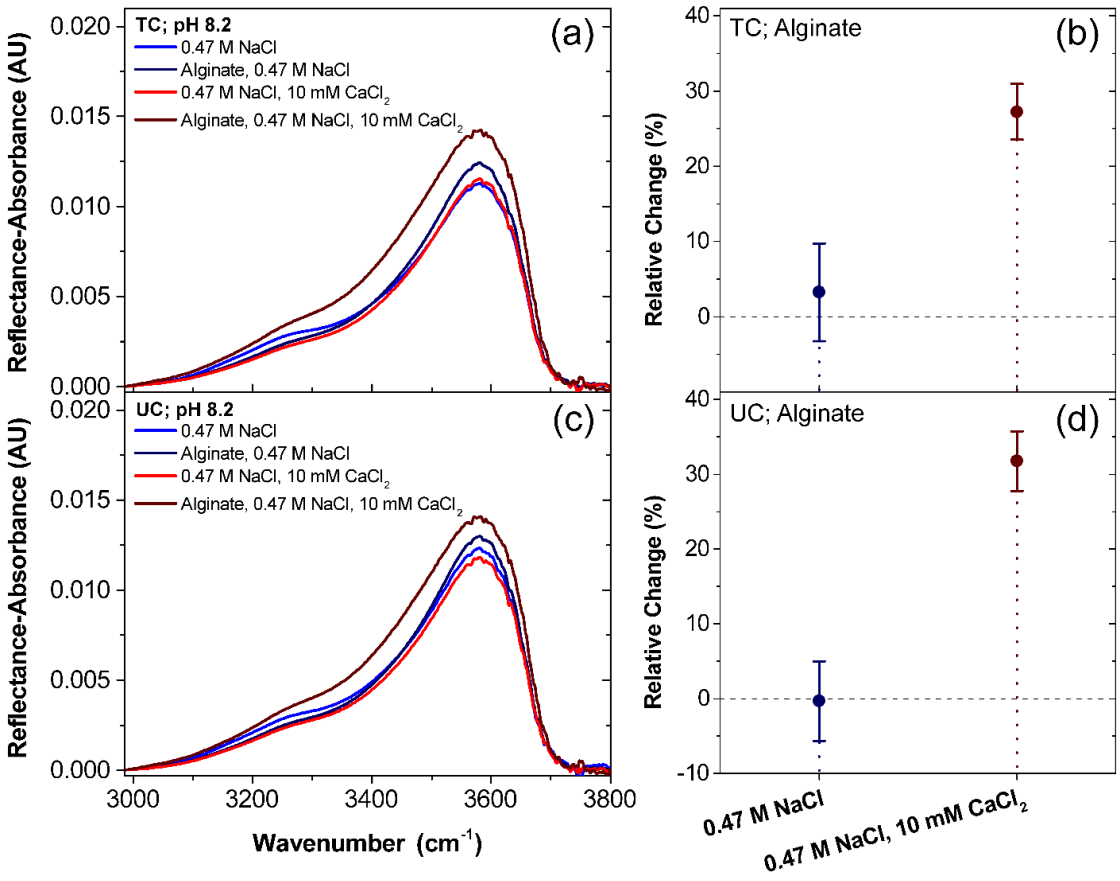

Fig. 1. IRRAS spectra of the OH stretching region and the corresponding relative changes in integrated peak area of the film indicate that $CaCl_2$ induces significant alginate co-adsorption to the d_{31}-palmitic acid monolayer. Data points and error bars are color-coded to indicate differences in solution composition. Surface pressure was held constant in the (a) tilted condensed (5 mN/m) and (c) untilted condensed (25 mN/m) phases throughout spectral acquisition. The relative changes in integrated peak area between the solutions with and without alginate are quantified in the (b) tilted condensed and (d) untilted condensed phases. Positive relative change indicates alginate co-adsorption to the monolayer, and 0% relative change indicates no co-adsorption.

Figs. 1a and 1c illustrate changes in the OH stretching region spectra caused by increasing organic surface coverage due to alginate co-adsorption. The spectrum of d_{31}-palmitic acid spread onto an aqueous solution containing 50 ppm alginate, 0.47 M NaCl, and 10 mM $CaCl_2$ is significantly enhanced relative to d_{31}-palmitic acid spread onto the salt water solution. IRRAS signal corresponding to the NaCl and alginate solution is slightly greater relative to the NaCl solution alone, but the differences are much smaller in the absence of $CaCl_2$. The IRRAS film

spectrum corresponding to alginate co-adsorption closely follows the shape of the monolayer spectrum on salt water solution, and the greatest OH stretching region signal enhancement occurs around ~3580 cm^{-1} which has been assigned to surface water molecules hydrogen bonded to a carboxylic acid group.[94,105,106] Therefore, alginate co-adsorption enhances the signal around 3580 cm^{-1} due to the alginate carboxylate hydration.

To better quantify organic surface coverage as a function of alginate co-adsorption, the MMA-corrected OH region was integrated between 2985 and 3800 cm^{-1}. The relative change in the integrated peak areas between the spectra with and without alginate was calculated using the following formula:

$$\text{Relative Change} = \frac{(A_{\text{Alginate}} - A_{\text{SW}})}{A_{\text{SW}}} \times 100\%. \quad (2)$$

In this equation, A_{Alginate} represents the integrated peak area of the spectrum with alginate in the solution, and A_{SW} represents the integrated peak area of the spectrum containing only salt water (no alginate) in the solution. Alginate co-adsorption corresponds to a positive relative change in surface coverage, and no adsorption results in a 0% relative change. While the 0.47 M NaCl solution might induce some alginate co-adsorption to the TC monolayer, as shown by the small but positive relative change value in Fig. 1b, the value is not statistically significant given that the error (represented as one standard deviation from the mean) is larger than the average relative change value. Addition of 10 mM $CaCl_2$ to the solution containing alginate induces a significant increase in the integrated peak area and consequently a 27% relative change in surface coverage. This increase suggests an alginate co-adsorption mechanism of divalent cationic bridging between alginate and d_{31}-palmitic acid carboxylate moieties.

The differences between the TC and UC spectra and associated relative changes in surface coverage provide insights into the co-adsorption mechanism. The UC film spectrum corresponding

to the 50 ppm alginate and 0.47 M NaCl solution nearly overlaps with the UC monolayer spectrum corresponding to the 0.47 M NaCl solution (Figure 1c), suggesting little to no alginate co-adsorption. The average relative difference in integrated peak area of the UC monolayer and film spectra is approximately 0% (Figure 1d), indicating a lack of alginate co-adsorption. Additionally, the slightly larger relative change in the TC spectrum surface coverage suggests that alginate expands the monolayer. It is possible that repulsive electrostatic interactions between the d_{31}-palmitic acid and alginate carboxylate moieties expand the monolayer, consequently increasing surface coverage in the TC phase. However, in the UC phase, increased dispersion interactions between the alkyl tails counteract the repulsive forces. This hypothesis is further supported by greater mean molecular area (MMA) expansion with alginate in the solution for the TC film relative to the UC film (see Table S1). Higher surface pressure increases alginate co-adsorption for the solution containing 10 mM $CaCl_2$ to a 32% relative change in surface coverage, and film expansion in the presence of alginate is not significantly different between the TC and UC phases. Thus, alginate likely does not intercalate between the d_{31}-palmitic acid molecules with $CaCl_2$ in the solution, and the UC film possibly provides more ideally spaced sites for the Ca^{2+} bridges.

Monolayer protonation impacts on alginate co-adsorption

Palmitic acid protonation state significantly impacts the extent of alginate co-adsorption. For the d_{31}-palmitic acid monolayer at pH 5.8, there is a reduced degree of alginate co-adsorption to the film in comparison to the chemical system at pH 8.2. The d_{31}-palmitic acid TC and UC spectra corresponding to the solution containing alginate have higher reflectance-absorbance values across the entire OH stretching region (Figs. 2a and 2c), indicative of alginate co-adsorption. The relative changes in surface coverage presented in Figs. 2b and 2d quantify this observation, in which alginate co-adsorption at pH 5.8 results in a 14% and 9% increase in the

integrated peak area for the TC and UC phase spectra, respectively. At pH 8.2, alginate co-adsorption results in a 27% and 32% integrated peak area increase for the TC and UC phase spectra, respectively. Therefore, increased d_{31}-palmitic acid protonation decreases the extent of alginate co-adsorption. Unlike the interfacial film at pH 8.2, monolayer compression decreases the magnitude of alginate co-adsorption for the solution at pH 5.8. Alginate might be expanding the TC film similarly to the mechanism proposed for the solution containing only 0.47 M NaCl.

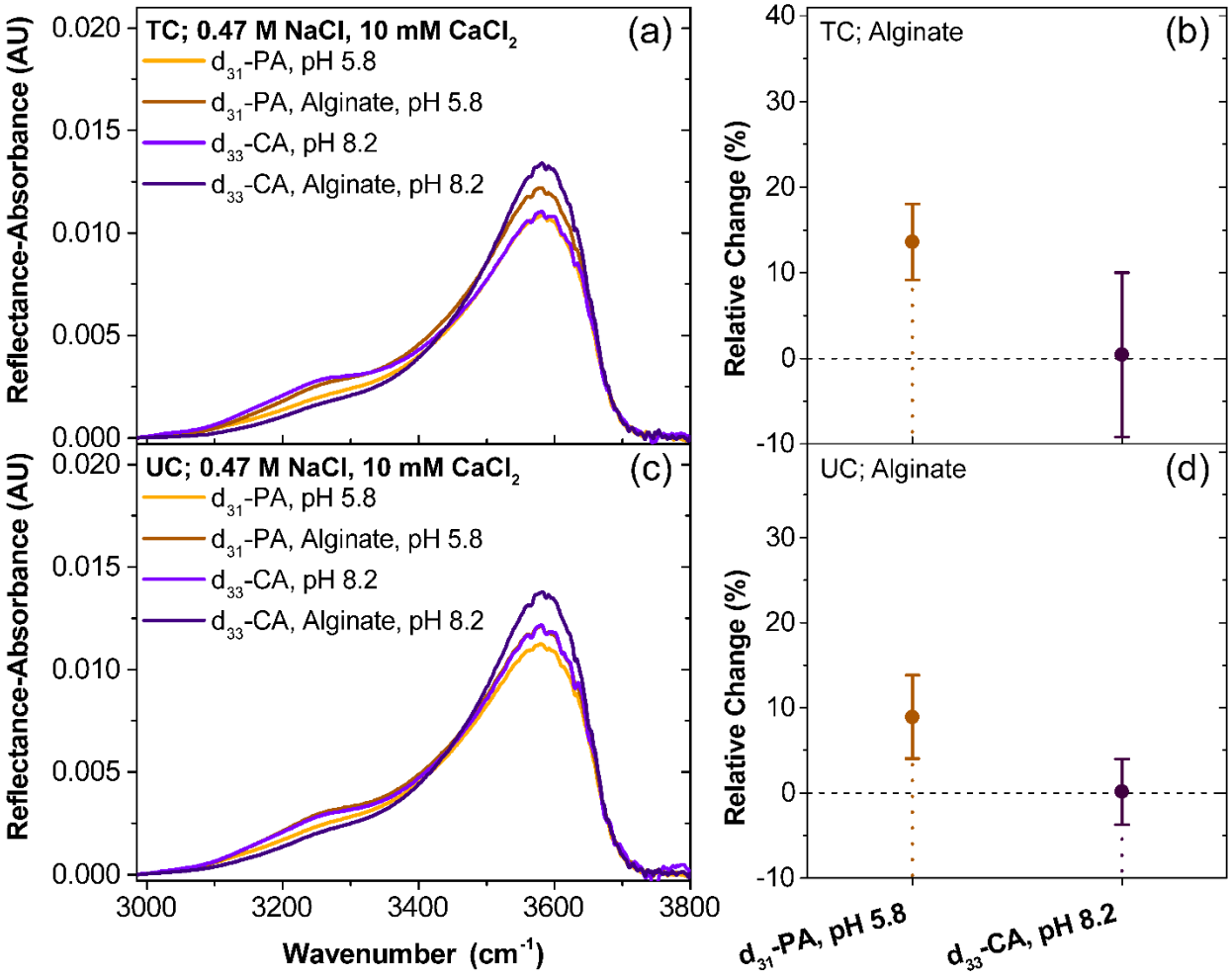

Fig. 2. IRRAS spectra of the OH stretching region and the corresponding relative changes in integrated peak area of d_{31}-palmitic acid (d_{31}-PA) and d_{33}-cetyl alcohol (d_{33}-CA) monolayers show that headgroup protonation prevents alginate co-adsorption. Data points and error bars are color-coded to indicate differences in monolayer and solution composition. Surface pressure was held

constant in the (a) tilted condensed (5 mN/m) and (c) untilted condensed (25 mN/m) phases throughout spectral acquisition. (Note that the light purple and dark brown data curves overlap in (c).) The relative changes in integrated peak area between the solutions with and without alginate are quantified in the (b) tilted condensed and (d) untilted condensed phases. Positive relative change indicates alginate co-adsorption to the monolayer, and 0% relative change indicates no co-adsorption.

A fully protonated d_{33}-cetyl alcohol monolayer was examined as a control because it does not become partially deprotonated in the presence of salts at any of the pH values tested. Trends in the IRRAS spectra of d_{33}-cetyl alcohol alone are less clear (Figs. 2a and 2c). In both monolayer phases, the alginate solution enhances IRRAS signal at ~3580 cm^{-1} and decreases the signal between ~3050 and 3440 cm^{-1} relative to the salt water solution. The region around 3050 cm^{-1} has been attributed to cyclic carboxylic acid dimers observed in polyacrylic acid solutions,[106,107] and the region from ~3200 cm^{-1} to ~3400 cm^{-1} corresponds to a more ordered hydrogen bonding structure to a less-ordered water structure.[105,108,109] Further analysis reveals no significant differences between the OH region integrated peak areas for the solutions with and without alginate in both the TC and UC phases, resulting in a 0% relative change in surface coverage (Figs. 2b and 2d). It is likely that alginate perturbs the interfacial hydration structure but does not co-adsorb to the cetyl alcohol monolayer. Thus, a protonated monolayer blocks alginate co-adsorption, indicating the importance of electrostatic interactions in polysaccharide co-adsorption to an SSML proxy film.

The carboxylic acid spectral region (1150-1850 cm^{-1}) provides further insight into the d_{31}-palmitic acid protonation state and the extent of alginate co-adsorption. Harmonic vibrational frequency calculations were performed to predict the relative frequency shifts between the d_{31}-palmitic acid carboxylate and carboxylic acid modes and the alginate carboxylate modes (see ESI Section S3). Additionally, peaks were fitted to Gaussian functions to resolve the center

wavelengths and full width at half maximum (FWHM) values; the fitting procedure and summary of the Gaussian fits for each spectrum are summarized in ESI Section S4. Spectra of a d_{31}-palmitic acid TC (Fig. 3a) and UC (Fig. 3c) monolayer exhibit four negative peaks corresponding to the lipid carboxylic acid moieties and one positive band at ~1660 cm^{-1} corresponding to the water bending mode (δ H-O-H). The protonated carboxylic acid moiety is characterized by the C-OH stretching mode (ν C-OH, ~1270 cm^{-1}) and the C=O stretching mode (ν C=O, ~1720 cm^{-1}). Deprotonation of the carboxylic acid leads to the appearance of the COO^- symmetric (ν_S COO^-, ~1410 cm^{-1}) and asymmetric (ν_{AS} COO^-, ~1540 cm^{-1}) stretching modes (negative bands).

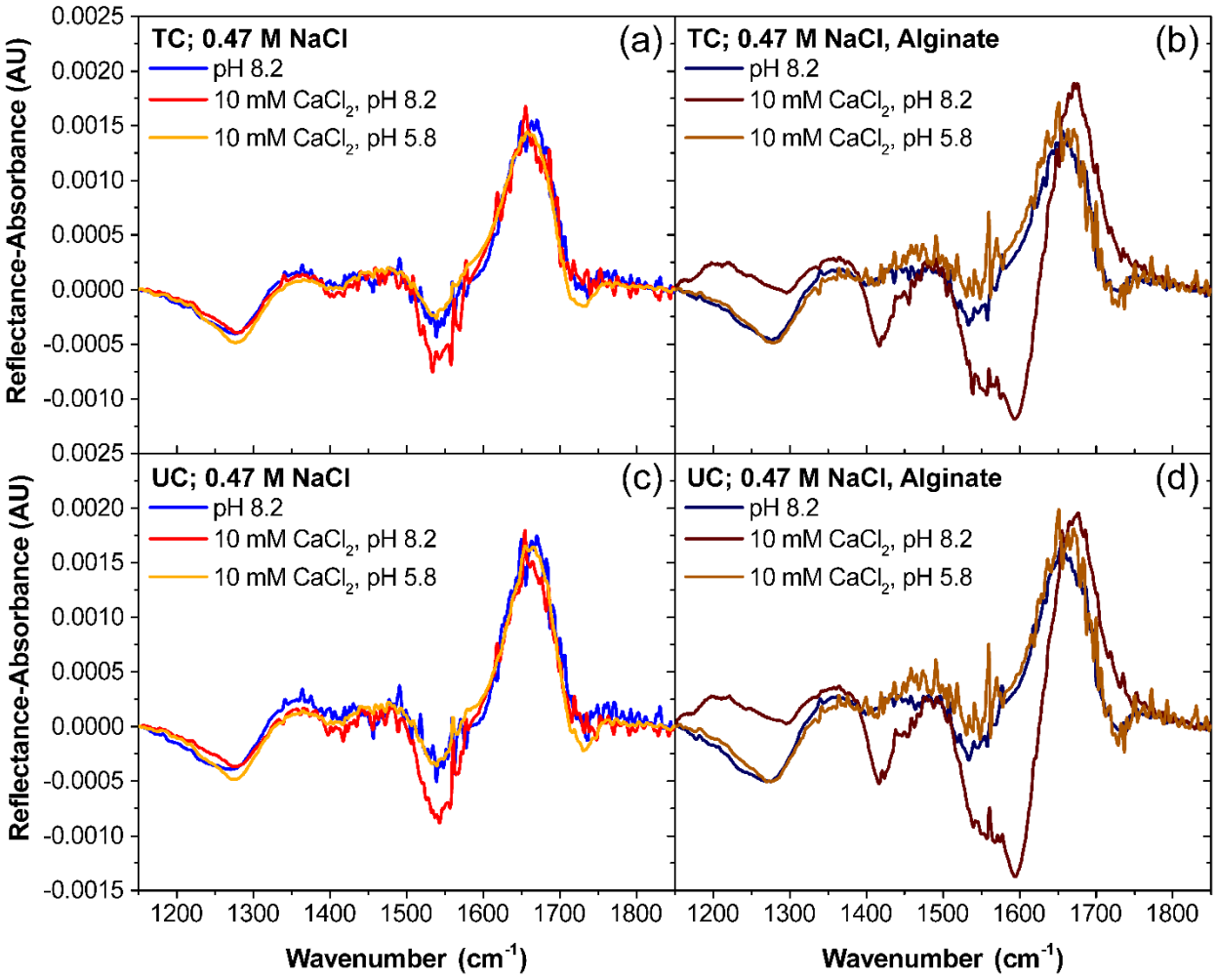

Fig. 3. IRRAS spectra of the COOH stretching region provide direct evidence of alginate co-adsorption via Ca^{2+} bridging interactions to the d_{31}-palmitic acid monolayer at pH 8.2. Spectral lines are color-coded to indicate differences in solution composition. Surface pressure was held constant in the (a), (b) tilted condensed (5 mN/m) and (c), (d) untilted condensed (25 mN/m) phases throughout spectral acquisition. Spectra corresponding to the salt water solutions are shown in (a) and (c), and spectra corresponding to the salt water solutions containing 50 ppm alginate are shown in (b) and (d).

As anticipated, d_{31}-palmitic acid spread onto a 0.47 M NaCl solution at pH 8.2 is partially deprotonated, demonstrated by the presence of all four carboxylic acid and carboxylate stretching modes (Figs. 3a and 3c). Addition of 10 mM $CaCl_2$ further deprotonates the headgroups, as shown by the increase in COO^- stretching intensities and by the disappearance of the C=O stretching mode in both TC and UC phases (Tables S6 and S8). Decreasing the pH to 5.8 increases the extent of d_{31}-palmitic acid protonation; the C-OH and C=O stretching modes are most intense at this pH (Table S10). However, the presence of the COO^- stretching modes in the TC and UC phase spectra indicates that Ca^{2+} induces some deprotonation which has been shown previously.[40,110–112]

Direct measurement of alginate co-adsorption to the d_{31}-palmitic acid monolayer is observed in Figs. 3b and 3d. There is a large increase in the negative COO^- stretching peak intensities and breadth for d_{31}-palmitic acid spread onto the 0.47 M NaCl, 10 mM $CaCl_2$, and 50 ppm alginate solution at pH 8.2. The asymmetric and symmetric stretches appear to split into higher and lower frequency bands, so an additional Gaussian function was used to fit both peaks (Fig. S6). Vibrational frequency calculations predict a 47 cm^{-1} blue shift and a 20 cm^{-1} blue shift for the alginate asymmetric and symmetric COO^- stretching modes, respectively, relative to the corresponding d_{31}-palmitic acid modes (Tables S3 and S5). The theoretical predictions quite closely match the experimental ~55 cm^{-1} blue shift for the second ν_{AS} COO^- peak and the ~37 cm^{-1} blue shift for the second ν_S COO^- peak (Table S9). Hence, the higher frequency COO^- stretching

bands indicate alginate co-adsorption to the largely deprotonated monolayer in the presence of $CaCl_2$.

The carboxylate region also provides evidence for Ca^{2+} ionic bridges driving alginate co-adsorption to the d_{31}-palmitic acid monolayer. Alginate co-adsorption induces d_{31}-palmitic acid deprotonation, as shown by increased COO^- stretching intensities and decreased C-OH stretching intensity for the pH 8.2 solution containing 10 mM $CaCl_2$ (Fig. 3). Similar peak broadening and intensity enhancement was observed for the phosphate headgroup vibrational modes of 1,2-dipalmitoyl-*sn*-glycero-3-phosphatidic acid (DPPA) upon arginine and guanidinium binding.[113] Palmitic acid deprotonation likely facilitates the formation of energetically favorable ionic complexes between alginate, Ca^{2+}, and palmitate. Furthermore, the ν_{AS} COO^-, ν_S COO^-, and ν C-OH modes blue shift upon addition of alginate to the solution (Table S9). The ν_{AS} COO^- mode blue shifts ~2.5 cm^{-1} in the TC phase but does not shift in the UC phase, the ν_S COO^- mode blue shifts 7 cm^{-1} in the TC phase and ~6 cm^{-1} in the UC phase, and the ν C-OH mode blue shifts ~13 cm^- in the TC phase and ~15 cm^{-1} in the UC phase. It is possible that the alginate carboxylate interacting with the Ca^{2+} ion complexed to the d_{31}-palmitate headgroup weakens ionic interactions between the monolayer carboxylate and the Ca^{2+} ion alone, thereby leading to an increased palmitic acid COO^- force constant and blue shifts in the palmitate carboxylate vibrational modes. However, it is more likely that the alginate carboxylate moieties further dehydrate the d_{31}-palmitate $\cdots$ Ca^{2+} complex upon alginate co-adsorption.

Spectra of d_{31}-palmitic acid spread onto the 0.47 M NaCl solution at pH 8.2 and the 0.47 M NaCl and 10 mM $CaCl_2$ solution at pH 5.8 do not exhibit any higher frequency COO^- stretching peaks upon alginate addition to the solution, suggesting minimal to no alginate co-adsorption (Fig. 3). Secondly, the ν_{AS} COO^-, ν_S COO^-, and ν C-OH mode peak areas are insignificantly

different between the solutions with and without alginate, meaning that alginate co-adsorption to the monolayer is unlikely (Tables S6 and S7; Tables S10 and S11). Smaller blue shifts in the ν_{AS} COO^-, ν_S COO^-, and ν C-OH modes are observed for the solutions containing 10 mM $CaCl_2$ and alginate at pH 5.8 as compared to the identical solution at pH 8.2 (Table S11). While these spectral shifts are not direct evidence of alginate co-adsorption to the monolayer, it is likely that alginate perturbs the d_{31}-palmitic acid headgroup hydration structure via electrostatic interactions with the headgroups. The less numerous d_{31}-palmitate headgroups may facilitate Ca^{2+} bridging interactions with alginate carboxylate moieties at various points across the monolayer, as also indicated by the small relative change in surface coverage (Figs. 2b and 2d). However, having fewer Ca^{2+} bridging sites hinders concerted alginate co-adsorption. For the d_{33}-cetyl alcohol monolayer (Figure S13), there are no detectable peaks corresponding to alginate carboxylate modes, further supporting the lack of alginate co-adsorption to the fully protonated monolayer.

Density and radial distribution profiles from MD simulations

Additional atomistic insights into the proposed divalent cationic bridging mechanism were obtained through explicit solvent all-atom molecular dynamics simulations of a TC palmitic acid monolayer at varying pH in the presence and absence of Ca^{2+} in the aqueous phase. Fig. 4 gives the number density and radial distribution profiles of selected species in each of the simulation conditions containing alginate at pH 8.2. The relative locations of the palmitic acid headgroups in the number density profiles (Figs. 4a and 4b) are in agreement with previous studies,[39,114] where the carboxylate headgroup of the palmitate sinks lower into the aqueous phase relative to the carboxylic acid. The peaks associated with the Ca^{2+} ion trace in Fig. 5a are indicative of selective calcium binding to the charged carboxylate headgroups. Similar coordination peaks associated with Na^+ are found in the sodium-only system shown in Fig. 4b.

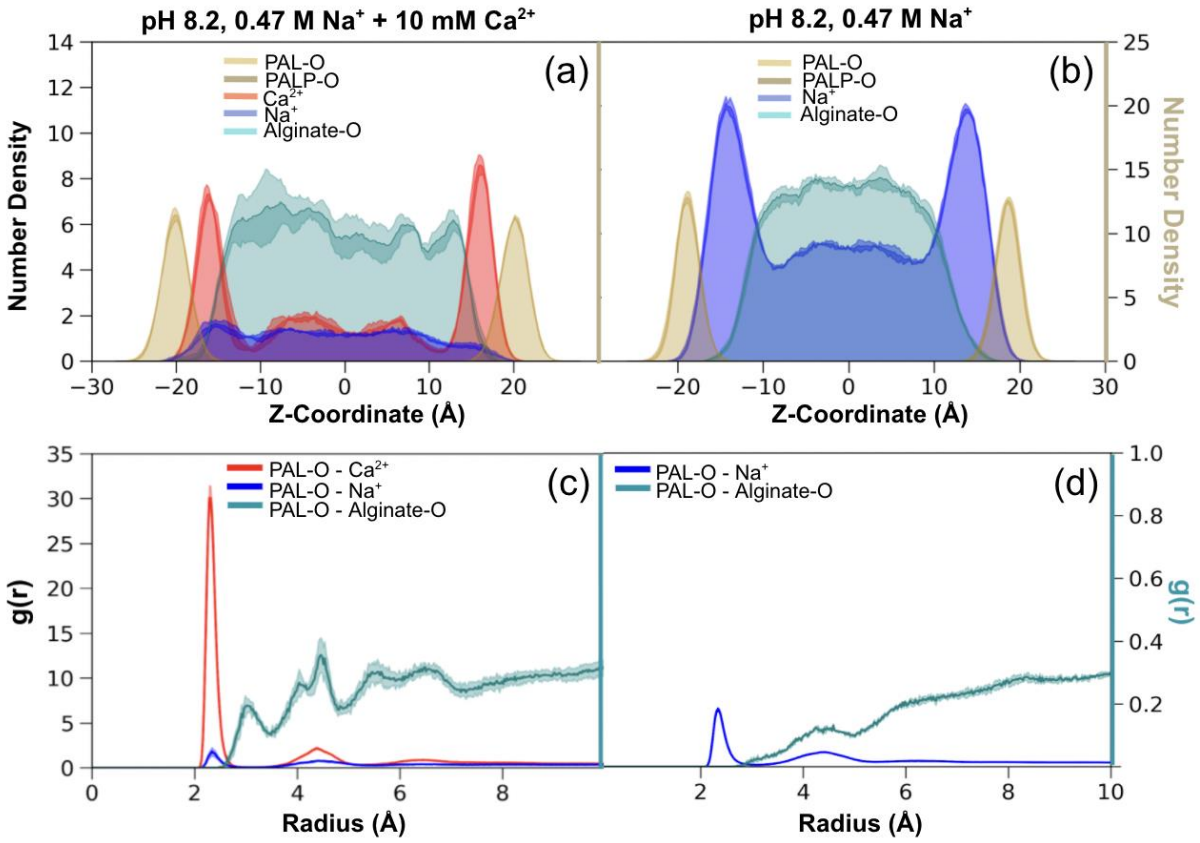

Fig. 4. Number density profiles (a, b) and radial distribution functions (c-d) of selected species from molecular dynamics simulations at pH 8.2 with a 0.47 M NaCl subphase either in the presence (a) or absence (b) of Ca^{2+}. In the number density profiles, the oxygen atom of the palmitate headgroup carboxylate (PAL-O) is used to represent the location of palmitate (light tan). The OH-oxygen atom of the palmitic acid headgroup (PALP-O) is used to represent the location of palmitic acid (dark tan). Similarly, a carboxylate oxygen atom on each M monomer in alginate (Alginate-O) is used to quantify the distribution of alginate (teal). The radial distribution functions of Ca^{2+}, Na^{+} and the alginate carboxylate with respect to the palmitate carboxylate are given for the systems in the presence (c) and absence (d) of Ca^{2+} at pH 8.2 over a 0.47 M NaCl subphase. Error representing ± 1 standard deviation are given by shaded regions above and below the average.

To determine whether alginate molecules co-adsorb to the monolayer by a cationic bridging mechanism as indicated by experiments, we can evaluate the alginate carboxylate traces. At pH 8.2, the alginate trace exhibits a broader, flatter profile in the presence of Ca^{2+} and a sharper rise in alginate coordination that occurs closer to the palmitate headgroups. We can also investigate this behavior using the radial distribution function (RDF) in which the probability density of the

cation (Ca^{2+} or Na^{+}) or functional group (alginate COO^{-}) as a function of distance (r) from the palmitate headgroup is plotted (Figs 4c-d). There is a sharp cation peak as expected at just over 2 Å in both systems. However, the alginate COO^{-} group exhibits distinctly different behavior between the two systems. The sharp peak at 3 Å in the presence of Ca^{2+} suggests that calcium likely serves as a bridge between the two COO^{-} moieties; conversely, in the absence of Ca^{2+}, the alginate peak occurs over much larger distances from the palmitate, has significantly lower probability, and is much broader. Furthermore, the RDFs of the water atoms (H_w and O_w) with respect to the palmitate COO^{-} are given in Fig. S14. The sharp H_w and O_w peaks at approximately 2 and 3 Å, respectively, are associated with the water hydration shell around the palmitate COO^{-} headgroup.[114] With Ca^{2+} coordination, the COO^{-} headgroups are significantly less hydrated in comparison to Na^{+}-coordinated headgroups, where the solvation shell trace is much stronger. This observation agrees with the d_{31}-palmitic acid ν_{AS} COO^{-}, ν_{S} COO^{-}, and ν C-OH vibrational mode blue shifts upon alginate co-adsorption, indicative of monolayer headgroup dehydration. Taken together, these results strongly suggest that Ca^{2+} enables the adsorption of alginate to the palmitic acid monolayer at pH 8.2 through a divalent cation bridge.

In comparison, we also provide the number density profiles and RDFs for the monolayer systems at pH 5.8 in which the monolayer is fully protonated (Figs. 5a-d). The number density plots exhibit distinctly different profiles from their higher pH counterparts; with Ca^{2+} present, rather than adsorbing to the surface, there is clear aggregation of the alginate in solution that is consistent with the gelation of alginate.[115–118] Without Ca^{2+}, the alginate shows a broader, flatter profile, indicating even distribution of alginate throughout solution and very little adsorption to the interface. The RDFs, in contrast with the higher pH system, show that alginates peak at just over 2 Å, which indicate that alginate weakly interacts with the monolayer via hydrogen bonding

or dispersive forces between the alginate COO^- and palmitic acid -OH. The small cation hump at the same radius can be attributed to contact-ion pairing at the double-bonded oxygen of the carboxylic acid.[39] The subsequent increase in cation density after 4 Å may be attributed to either solvent-shared ion pairing between the cations and the first hydration shell of the headgroups, or, more likely, to contact-ion pairing between the cations and the alginate COO^-. These results are consistent with the experimental findings presented above, which suggest that palmitic acid protonation hinders alginate co-adsorption.

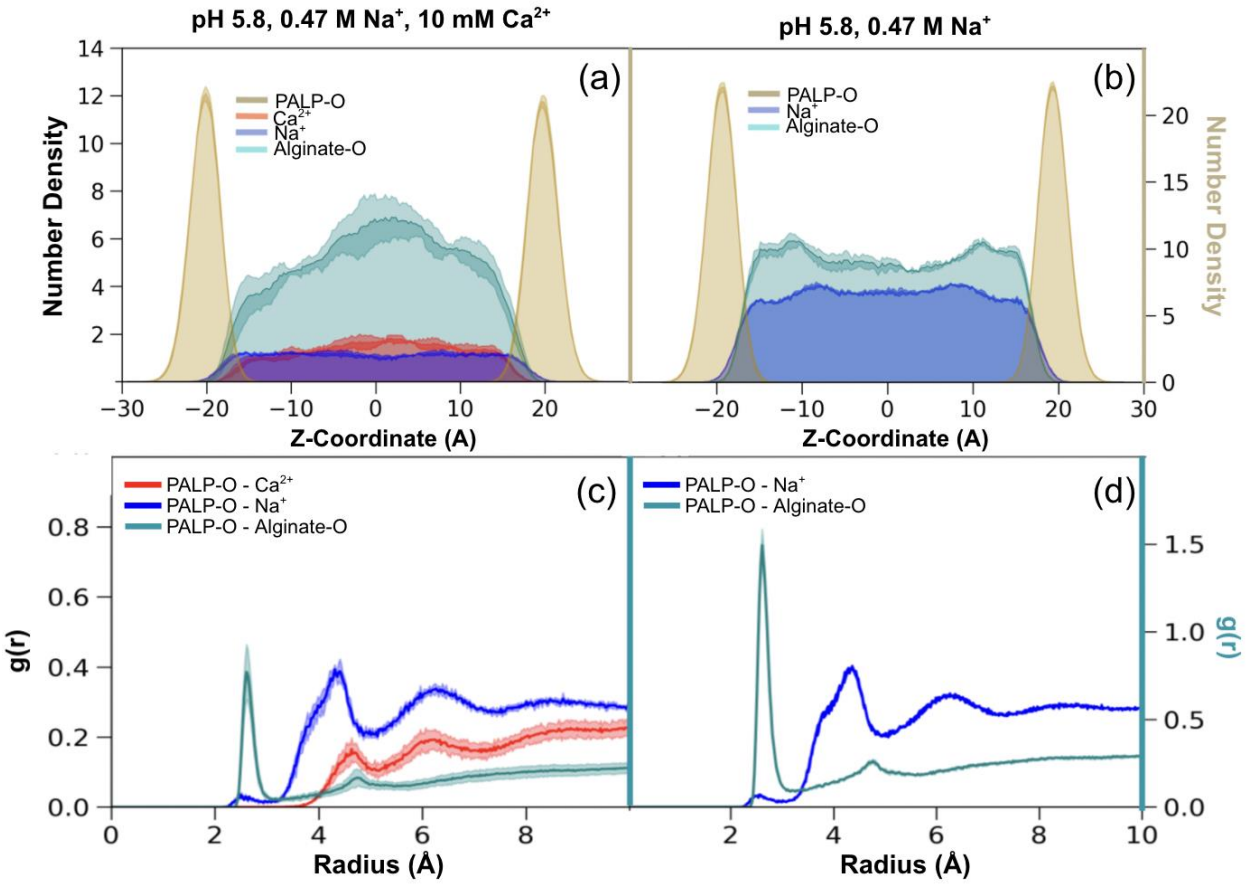

Fig. 5. Number density (a-b) and radial distribution functions (c-d) from molecular dynamics simulations at pH 5.8 in which the palmitic acid monolayer is fully protonated. Error representing ±1 standard deviation are given by shaded regions above and below the average.

Impacts of alginate co-adsorption on palmitic acid interfacial structure

To determine if alginate co-adsorption perturbs d_{31}-palmitic acid interfacial organization, the CD_2 scissoring mode was analyzed as a function of solution composition, pH, and surface pressure (Fig. 6). All conditions yield a CD_2 scissoring mode center wavelength of 1089 cm^{-1} (see Table S16), indicative of hexagonal lattice packing structure.[119] Furthermore, the absence of perturbations in the lattice packing structure, regardless of alginate presence in solution, indicates that alginate does not intercalate into the film. CD_2 scissoring mode spectra corresponding to the salt water and alginate solutions directly overlap for the 0.47 M NaCl solution at pH 8.2 (Figs. 6a and 6d) and for the 0.47 M NaCl and 10 mM $CaCl_2$ solution at pH 5.8 (Figs. 6c and 6f), further indicating no alginate co-adsorption. However, the CD_2 scissoring mode reflectance-absorbance signal magnitude in the TC and UC phase is significantly enhanced for d_{31}-palmitic acid spread onto the 0.47 M NaCl, 10 mM $CaCl_2$, and 50 ppm alginate solutions at pH 8.2 (Figs. 6b and 6e). Signal enhancement is most apparent in the high frequency regime, and a smaller extent of signal enhancement occurs in the lower frequency region of the spectra. From the harmonic frequency analysis results (Tables S3 and S5), the signal enhancement can be attributed to alginate C-OH stretching and bending and CH stretching. The CD_2 shoulder features overlap in frequency with the CD_2 scissoring modes, and particularly intense alginate vibrational transitions occur ~10 cm^{-1} lower than and ~20 cm^{-1} higher than the center frequency of the d_{31}-palmitate CD_2 scissoring mode. As a result, the signal enhancement surrounding the CD_2 scissoring peak can be confidently attributed to alginate co-adsorption to the monolayer via Ca^{2+} bridging interactions.

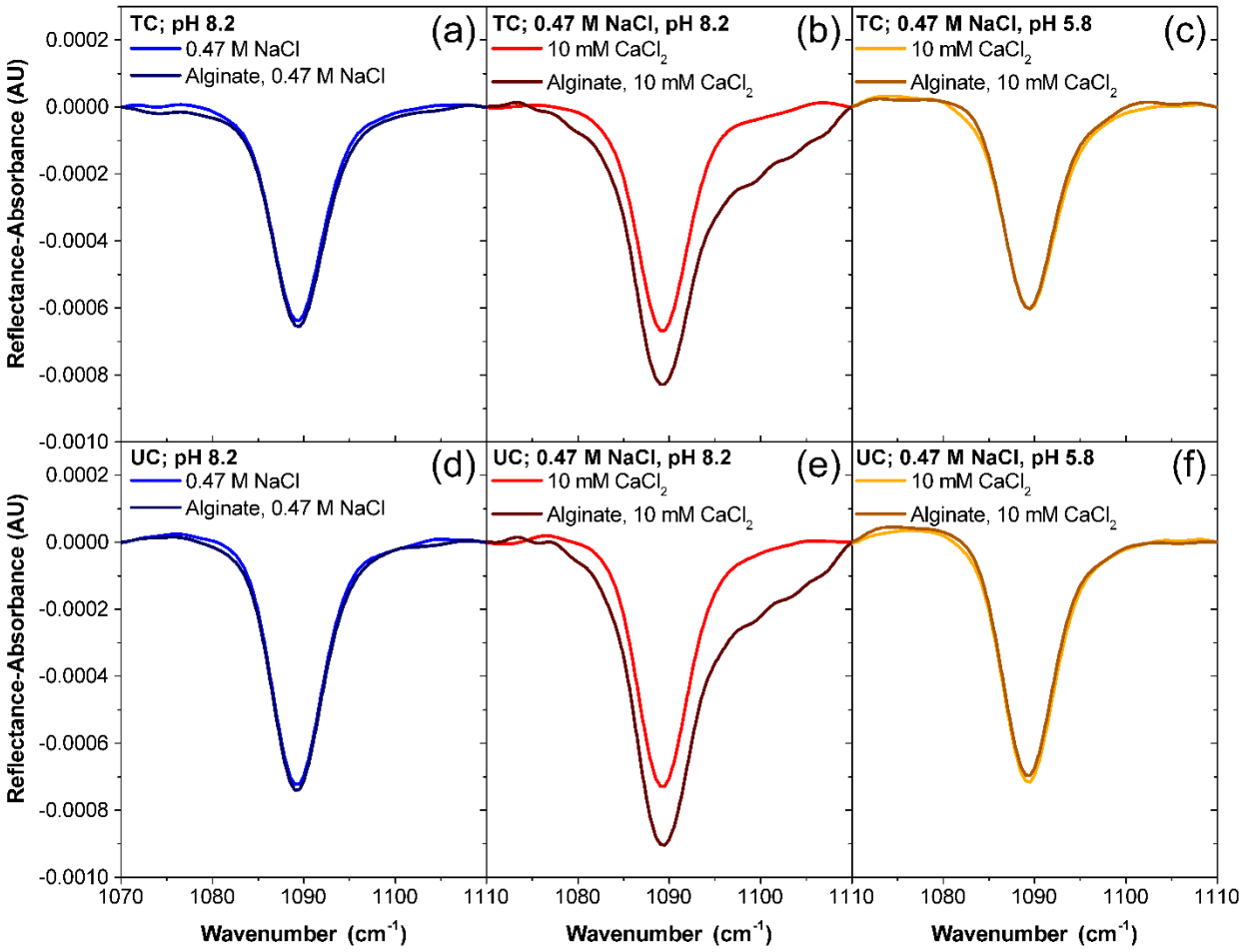

Fig. 6. IRRAS spectra of the CD_2 scissoring mode region demonstrate alginate co-adsorption to the d_{31}-palmitic acid monolayer in the presence of 10 mM $CaCl_2$ at pH 8.2, and the spectra indicate no changes in d_{31}-palmitic acid lattice packing upon adsorption. Spectral lines are color-coded to indicate differences in solution composition. Surface pressure was held constant in the (a), (b), (c) tilted condensed (5 mN/m) and (d), (e), (f) untilted condensed (25 mN/m) phases throughout spectral acquisition.

The C-D stretching region provides further evidence for the lack of alginate intercalation into the palmitic acid monolayer. Regardless of alginate presence, the stretching mode center frequencies remain the same for the 0.47 M NaCl solution at pH 8.2 (Figs. S15a and S15d), the 0.47 M NaCl and 10 mM $CaCl_2$ solution at pH 8.2 (Figs. S15b and S15e), and the 0.47 M NaCl and 10 mM $CaCl_2$ solution at pH 5.8 (Figs. S15c and Figs. S15f). Alginate intercalation would disrupt d_{31}-palmitic acid packing within the monolayer, reducing intermolecular interactions

between the lipid tails and manifesting as a blue-shift in the C-D stretching modes. No such spectral shift is observed upon alginate co-adsorption, indicating that alginate is confined to the subsurface region. The peak intensities are also the same within experimental error; however, any quantitative analysis of the intensities is forgone due to known impacts of vibrational excitons on surfactant hydrocarbon peak intensities, particularly in the UC phase.[120]

Molecular dynamics simulations were also used to investigate the impacts of alginate co-adsorption to the interfacial organization of the monolayer. The number density plots show that, for all systems, the alginate trace goes to zero as the monolayer headgroup densities increase. Thus, there is little to no alginate intercalation into the monolayer; alginate remains largely in the subsurface region, which is in good agreement with the experimental observation that hexagonal packing structure of the palmitic acid chains is preserved upon alginate co-adsorption.

Local order parameters were extracted from molecular dynamics simulations (Fig. 7 and Fig. S16) to further understand the impacts of alginate adsorption on the dynamics and organization of the palmitic acid monolayer,. These order parameters are calculated by

$$S_{CD} = \frac{3\times\langle cos^2\theta\rangle - 1}{2}, \quad (3)$$

where θ is the angle between the vector normal to the surface and adjacent carbon atoms, C_{n-1} and C_{n+1}. A high order parameter indicates high ordering among the alkyl chains with low motional anisotropy. Fig. S16 gives the order parameters for the palmitic acid and palmitate chains of the monolayers with and without alginate in the aqueous phase. With the exception of carbons 2 and 15, which tend to have low order parameters due to their geometric positions at the top and bottom of the monolayer, the order parameters remain relatively constant at low pH, indicating similar levels of ordering across the alkyl chains and thus no significant perturbations due to alginate interaction. However, at high pH, the order parameters vary across the chain. Additionally, the

presence of alginate slightly decreases the order parameters, with the largest decrease seen in the absence of Ca^{2+}. Finally, compared to the low pH systems in which the order parameters steadily decrease from C4 to C2, the relative orders between C2 and C3 are reversed at high pH with C2 having a higher order parameter than C3. This reversal indicates that the headgroup carbons experience increased rotational rigidity at high pH.

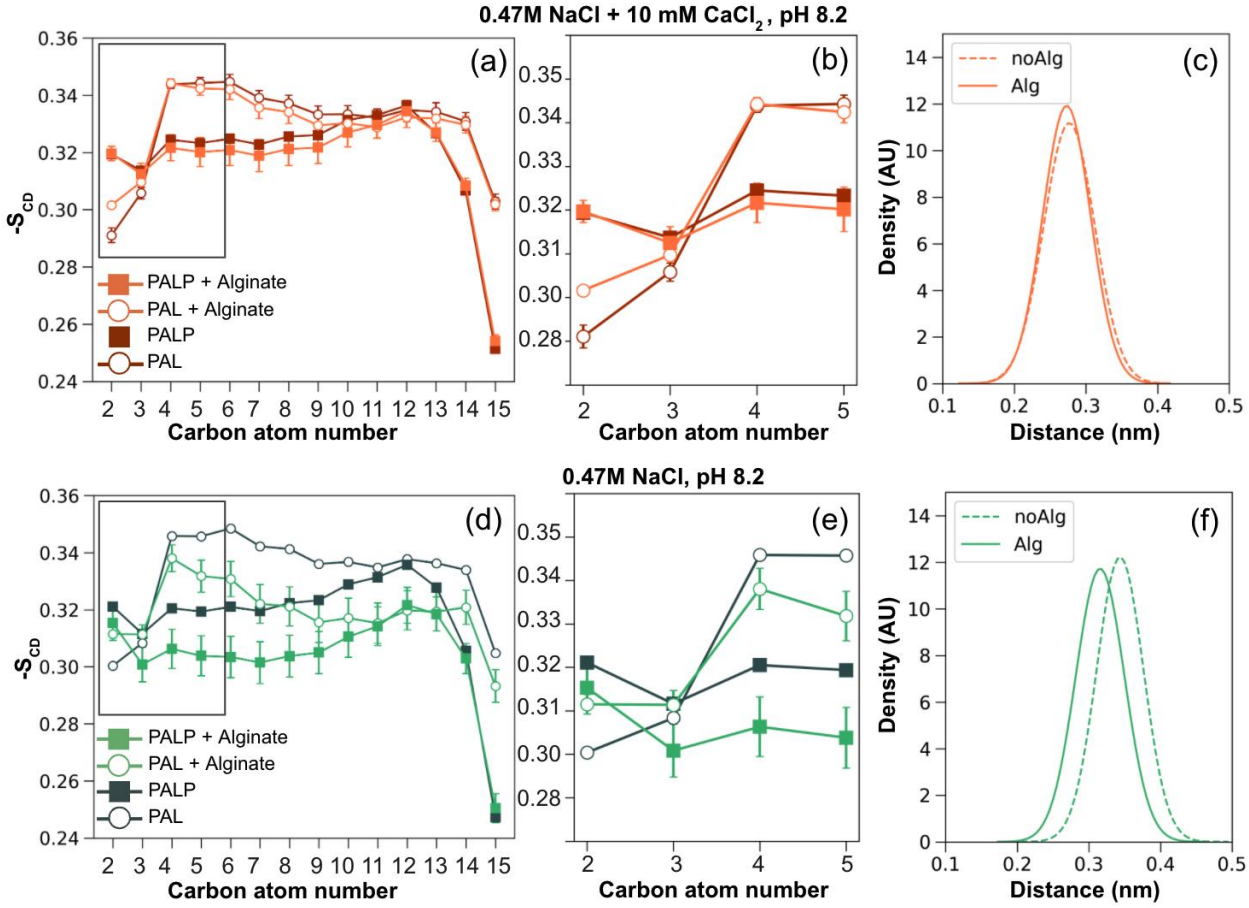

Fig 7. Local order parameters (a-b, d-e) and headgroup separation (c, f) for palmitic acid monolayers at pH 8.2 in the presence (a-c) and absence (d-f) of calcium. Order parameters are calculated based on protonation state for all systems with and without alginate. Figures b and e are specific to the C2-C4 carbon range in the presence and absence of calcium, respectively.

To understand the physical basis of these structural differences, we recalculated order parameters based on residue protonation state (Fig. 7). In all systems at pH 8.2, the deprotonated palmitic acid shows higher ordering than the protonated form, and the addition of alginate

generally decreases ordering with the exception of C2 in both cases (Figs 7a and 7d). In the presence of Ca^{2+}, alginate adsorption appears to increase ordering of the carboxylate groups but has no effect on the ordering of the protonated form (Fig 7b). In the absence of Ca^{2+}, the addition of alginate similarly increases ordering of the palmitate carboxylate headgroups but decreases ordering of the acid (Fig 7e).

To understand the differences in ordering based on headgroup protonation, we plotted the variations in headgroup position within the monolayer. Recalling that the palmitate headgroup tends to sink further into the aqueous phase in comparison to the palmitic acid, in Figs. 7c and 7f we provide distributions of the height differences between carboxylate and carboxylic acid headgroups. The carboxylates are drawn into the aqueous phase, where they experience stabilizing ion-pairing with the cations, but the magnitude of the separation varies based on cation type. In the presence of Ca^{2+}, the headgroup separation decreases by nearly 1 Å to 2.8 Å, down from 3.8 Å without Ca^{2+}. The smaller difference in headgroup positions can be attributed to calcium-induced monolayer compression; Ca^{2+} binds neighboring carboxylate headgroups, thereby effectively shielding repulsive negative charges and bringing the headgroups closer together. Monovalent sodium does not participate in the ionic bridging and does less to screen the charges. Furthermore, whether alginate impacts the headgroup separation depends on the dominant adsorption or interaction mechanism. Because alginate adsorbs to the monolayer via calcium ion bridging, adsorption does not impact headgroup separation. However, without Ca^{2+} present, it is possible that the alginate COO^- slightly destabilizes the palmitate headgroups through repulsive interactions that are less mediated by Na^+, expanding the monolayer and allowing more space for the headgroups to align. Indeed, monolayer expansion is observed experimentally with increased MMA upon alginate adsorption (Table S1).

The differences in headgroup position between the protonated and deprotonated forms can explain the trends associated with the overall increase in ordering at the C2 carbon that are not seen in low pH systems. With the carboxylic acid headgroup more embedded into the monolayer, the rotational motion of that headgroup is significantly restricted, thus increasing the order parameter. Conversely, the carboxylate headgroups exposed to the aqueous phase experience a wider range of motion, and their order parameter decreases. In the case of alginate binding in the presence of Ca^{2+}, alginate has no impact on the carboxylic acids that are more deeply situated in the monolayer, but increases order associated with the carboxylates via the formation of calcium ion bridges that increase monolayer rigidity and decrease headgroup motion. In the case of alginate interacting with the monolayer without calcium bridges, we see a similar increase in order associated with the carboxylates and a decrease in order associated with the carboxylic acids. The mechanism for this behavior, although similar to that in calcium, is more likely explained by the decrease in headgroup separation associated with alginate interaction; the exposure of palmitic acid headgroups to the aqueous phase decreases order of the protonated form while at the same time increasing order of the carboxylate.

Magnesium bridging

With complementary insights gained into the divalent cationic bridging mechanism from both theory and experiment, the same alginate co-adsorption experiments were performed with $MgCl_2$, the most abundant divalent cation in seawater (~53 mM).[92,93] Mg^{2+} has such a strong hydration shell that the fully hydrated Mg^{2+} only weakly interacts with the alginate and palmitic acid carboxylate moieties.[67–70,105,112] Both 10 mM and 53 mM $MgCl_2$ solutions increase IRRAS reflectance-absorbance for the alginate-containing spectra at ~3580 cm^{-1}, and the magnitude of the signal increase is similar (Figs. 8a and 8c). Calculation of the relative change reveals that the higher

$MgCl_2$ concentration causes a marginal increase in alginate co-adsorbed to the d_{31}-palmitic acid monolayer (Figs. 8b and 8d). With increasing $MgCl_2$ concentration, the relative change in integrated peak area increases from 8% to 10% and from 3% to 9% in the TC and UC phases, respectively. The reduction in OH region relative change with film compression (TC to UC phase) further suggests weak binding. Mg^{2+} is not as efficient in shielding the palmitic acid carboxylate moieties from negatively charged alginate carboxylate moieties, yielding monolayer expansion and increased surface coverage in the TC phase. Film compression to the UC phase reduces the extent of available space for monolayer expansion, and increased dispersion forces between the lipid tails counterbalance the repulsive electrostatic interactions. Despite Mg^{2+} being ~5 times more abundant than Ca^{2+} in seawater, alginate co-adsorption mediated by Mg^{2+} is ~3 times weaker in comparison to Ca^{2+} when comparing seawater relative concentrations of 10 mM Ca^{2+} and 53 mM Mg^{2+}. At 10 mM concentrations for both cations, Ca^{2+} outperforms Mg^{2+} by a factor of ~3 in the TC phase and by a factor of ~10 in the UC phase (Figs. 1 and 8).

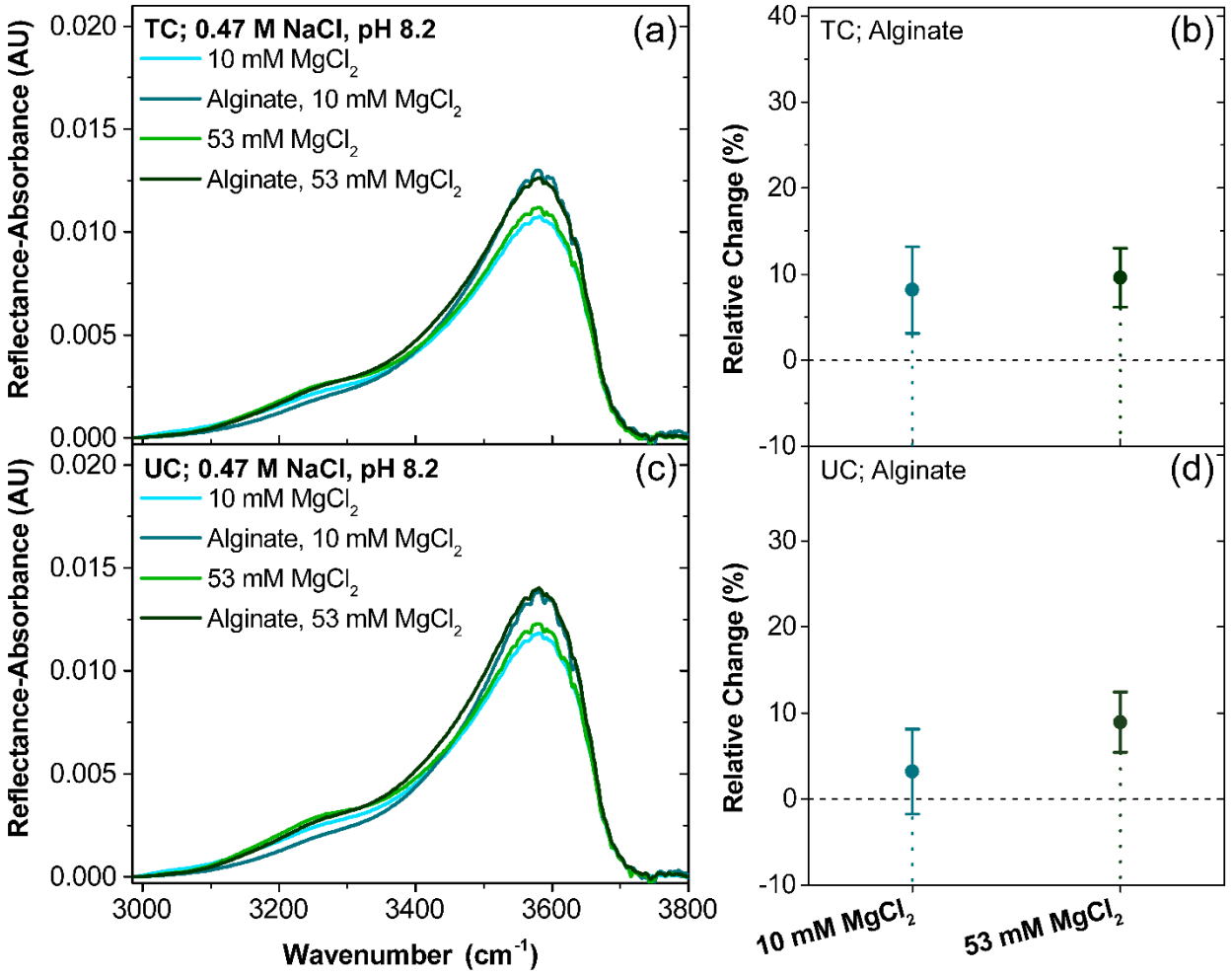

Fig. 8. IRRAS spectra of the OH stretching region and the corresponding relative changes in integrated peak area indicate that Mg^{2+} induces weak alginate co-adsorption to the d_{31}-palmitic acid monolayer. Data points and error bars are color-coded to indicate differences in solution composition. Surface pressure was held constant in the (a) tilted condensed (5 mN/m) and (c) untilted condensed (25 mN/m) phases throughout spectral acquisition. The relative changes in integrated peak area between the solutions with and without alginate are quantified in the (b) tilted condensed and (d) untilted condensed phases. Positive relative change indicates alginate co-adsorption to the monolayer, and 0% relative change indicates no co-adsorption.

The carboxylate region provides additional support for this weak Mg^{2+} bridging co-adsorption mechanism (Fig. S17). For d_{31}-palmitic acid spread onto the solution containing 10 mM $MgCl_2$, the ν_S COO^- mode is blue-shifted by 1 cm^{-1} in the TC phase and ~2.5 cm^{-1} in the UC phase, and the ν_{AS} COO^- mode is red-shifted by 1 cm^{-1} in the TC phase and ~3 cm^{-1} in the UC phase

(Tables S8 and S9). These small spectral shifts suggest that the d_{31}-palmitate carboxylate headgroup becomes dehydrated with the addition of alginate to the solution,[99] perhaps via complexation of Mg^{2+} to the d_{31}-palmitate carboxylate moiety. The integrated carboxylate peak areas do not change significantly between the salt water solution and alginate solution (Tables S12 and S13), suggesting no alginate co-adsorption.

Increasing the solution $MgCl_2$ concentration to 53 mM leads to some features of alginate co-adsorption to the monolayer (Fig. S17). The d_{31}-palmitic acid ν_{AS} COO^-, ν_S COO^-, and ν C-OH modes blue shift upon alginate addition to the solution (Tables S14 and S15), similarly to the spectra corresponding to the solutions containing 10 mM $CaCl_2$. The ν_{AS} COO^- blue shifts ~0.5 cm^{-1} in the TC phase and ~3 cm^{-1} in the UC phase, the ν_S COO^- blue shifts ~4 cm^{-1} in the TC phase and ~5 cm^{-1} in the UC phase, and the ν C-OH blue shifts ~9 cm^{-1} in the TC phase and ~12 cm^{-1} in the UC phase. The blue shifts are smaller than those observed with the 10 mM $CaCl_2$ solution at pH 8.2, either an indication of fewer Mg^{2+} bridging interactions or weaker bridging interactions. Secondly, the ν C-OH peak area decreases while the ν_{AS} COO^- and ν_S COO^- peak areas increase with alginate present in the solution, further supporting the hypothesis of alginate co-adsorption.

The CD_2 scissoring modes of d_{31}-palmitic acid spread onto the $MgCl_2$ solutions corroborate the findings from the OH stretching and COOH stretching regions. At 10 mM $MgCl_2$, the salt water and alginate spectra nearly overlap (Figs. S18a and S18c). There is a small increase in peak intensity of the TC spectrum corresponding to the alginate solution that could be attributed to alginate weakly co-adsorbed to the TC monolayer. Then the alginate is squeezed out upon film compression, causing the peak intensity difference to disappear in the UC phase. The solution containing 53 mM $MgCl_2$ and alginate induces increased peak intensities in the d_{31}-palmitic acid

CD_2 scissoring mode and the higher frequency regime relative to the spectra corresponding to the salt water solution (Figs. S18b and S18d). The signal enhancement is smaller in comparison to the system containing 10 mM $CaCl_2$ and alginate at pH 8.2, but the spectral trends match. Hence, the higher concentration of $MgCl_2$ facilitates some alginate co-adsorption to the monolayer through Mg^{2+} bridging interactions.

Both the CD_2 scissoring modes (Fig. S18) and the C-D stretching modes (Fig. S19) of d_{31}-palmitic acid spread onto the $MgCl_2$ solutions demonstrate that alginate does not intercalate into the monolayer. The center wavelengths of the CD_2 scissoring modes (Table S16) remain centered at 1089 cm^{-1}, indicating that alginate presence in the aqueous solution does not disrupt the hexagonal lattice packing of the monolayer.[119] The C-D stretching mode center wavelengths do not change between the salt water and alginate solutions as well, showing that the lipid film structure remains the same. Thus, alginate co-adsorption is confined to the region below the palmitic acid headgroups.

Conclusions

We directly observe alginate co-adsorption to an insoluble d_{31}-palmitic acid monolayer via divalent cationic bridging interactions using surface-sensitive infrared reflection-absorption spectroscopy (IRRAS) and molecular dynamics simulations. Fig. 9 summarizes the alginate co-adsorption mechanism. Ca^{2+} facilitates the greatest extent of alginate co-adsorption, as shown by the appearance of alginate vibrational modes in the IRRAS spectra and by the ~27% and ~32% increase in surface coverage in the tilted condensed (TC, 5 mN/m) and untilted condensed (UC, 25 mN/m) monolayer phases, respectively. Alginate co-adsorption is dependent upon d_{31}-palmitic acid protonation state, however; d_{31}-palmitate promotes alginate co-adsorption in the presence of

divalent cations, whereas protonation inhibits co-adsorption. Na^+ cations alone are insufficient in facilitating co-adsorption. Mg^{2+} induces ~3 times weaker alginate co-adsorption at a seawater concentration of 53 mM in comparison to 10 mM Ca^{2+}, and Mg^{2+} induces minimal co-adsorption when matching the Ca^{2+} seawater concentration (10 mM). The hydration free energy of Mg^{2+} is much higher than that of Ca^{2+}, meaning that Mg^{2+} cannot shed its hydration shell as readily to facilitate bridging interactions between the d_{31}-palmitate and alginate carboxylate moieties. The presence of alginate perturbs the hydration structure and dehydrates the d_{31}-palmitic acid carboxylic acid headgroups, but alginate co-adsorption does not change the d_{31}-palmitic acid lattice packing structure. Because alginate co-adsorption is largely confined to the subsurface region of the film, surface pressure plays a minimal role in the extent of alginate co-adsorption.

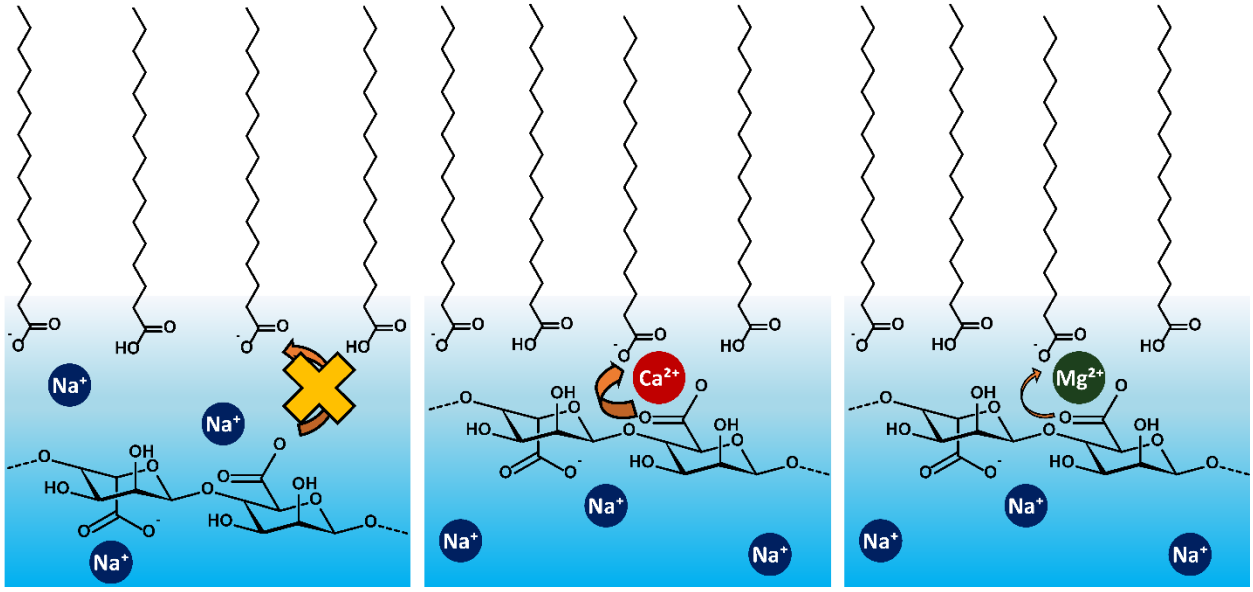

Fig. 9. A graphical summary of the alginate co-adsorption mechanism to a palmitic acid monolayer. Na^+ cations alone do not facilitate alginate co-adsorption. Alginate is co-adsorbed via a divalent cationic bridging interaction in which either Ca^{2+} or Mg^{2+} links the carboxylate moieties of alginate and palmitic acid. Ca^{2+} facilitates significant alginate co-adsorption, whereas alginate is weakly co-adsorbed in the presence of Mg^{2+}.

Our detailed experimental and computational characterization of the divalent cationic bridging interactions driving alginate co-adsorption to a sea surface microlayer (SSML) proxy film provides important physical and chemical insights into the potential mechanisms responsible for polysaccharide enrichment in sea spray aerosol (SSA). Ca^{2+} drives this bridging motif between the alginate and palmitic acid carboxylate moieties and outcompetes Mg^{2+} despite higher Mg^{2+} concentrations in seawater. Our findings corroborate the recent work of Cravigan *et al.* in which the authors measure Ca^{2+} enrichment in marine aerosol along with a large proportion of hydroxyl functional groups and low alkane-to-hydroxyl ratios, suggesting polysaccharide enrichment in SSA via Ca^{2+} bridging.[33] Quantifying polysaccharide co-adsorption to an interfacial film with IRRAS could provide useful empirical parameters to improve the representation of polysaccharides in marine aerosol climate models, and additional model systems comprised of polysaccharides with varying structure and functional groups need to be studied. We demonstrate that soluble polysaccharides interact electrostatically with other surface-active organic matter through seawater ionic bridging interactions, which can lead to polysaccharide surface enrichment in the SSML, and therefore, in SSA.

Author contributions

K.A.C.-F. designed the study, and H.C.A. and R.E.A. supervised the project and acquired funding. K.A.C.-F., M.E.F., and J.K. performed the experiments. A.C.D. performed the molecular dynamics simulations, and K.A.C.-F. performed the quantum chemistry calculations. K.A.C.-F. and A.C.D. analyzed the data and wrote the paper with input from all authors.

Conflicts of interest

The authors declare no conflicts of interest.

Acknowledgements

All authors acknowledge funding from the National Science Foundation Center for Aerosol Impacts on Chemistry of the Environment (NSF-CAICE) under Award No. CHE-1801971. Quantum chemistry calculations were performed at the Ohio Supercomputer Center under Project Number PAS1711. We thank Kevin Carter-Fenk for assistance with the vibrational frequency calculations. We also thank Nicholas Wauer for helpful discussions.

References

1 L. N. Hawkins and L. M. Russell, *Adv. Meteorol.*, 2010, **2010**, 1–14.
2 L. M. Russell, L. N. Hawkins, A. A. Frossard, P. K. Quinn and T. S. Bates, *Proc. Natl. Acad. Sci. U.S.A.*, 2010, **107**, 6652–6657.
3 J. Y. Aller, J. C. Radway, W. P. Kilthau, D. W. Bothe, T. W. Wilson, R. D. Vaillancourt, P. K. Quinn, D. J. Coffman, B. J. Murray and D. A. Knopf, *Atmos. Environ.*, 2017, **154**, 331–347.
4 S. Elliott, S. M. Burrows, C. Deal, X. Liu, M. Long, O. Ogunro, L. M. Russell and O. Wingenter, *Environ. Res. Lett.*, 2014, **9**, 064012.
5 Q. Gao, C. Leck, C. Rauschenberg and P. A. Matrai, *Ocean Sci.*, 2012, **8**, 401–418.
6 T. Jayarathne, C. M. Sultana, C. Lee, F. Malfatti, J. L. Cox, M. A. Pendergraft, K. A. Moore, F. Azam, A. V. Tivanski, C. D. Cappa, T. H. Bertram, V. H. Grassian, K. A. Prather and E. A. Stone, *Environ. Sci. Technol.*, 2016, **50**, 11511–11520.
7 D. C. O. Thornton, S. D. Brooks and J. Chen, *Front. Mar. Sci.*, 2016, **3**, 1–14.
8 E. S. Hasenecz, T. Jayarathne, M. A. Pendergraft, M. V. Santander, K. J. Mayer, J. Sauer, C. Lee, W. S. Gibson, S. M. Kruse, F. Malfatti, K. A. Prather and E. A. Stone, *ACS Earth Space Chem.*, 2020, **4**, 1638–1649.
9 E. Rastelli, C. Corinaldesi, A. Dell'Anno, M. Lo Martire, S. Greco, M. Cristina Facchini, M. Rinaldi, C. O'Dowd, D. Ceburnis and R. Danovaro, *Sci. Rep.*, 2017, **7**, 11475.
10 S. R. Schill, S. M. Burrows, E. S. Hasenecz, E. A. Stone and T. H. Bertram, *Atmosphere*, 2018, **9**, 476.
11 A. D. Estillore, H. S. Morris, V. W. Or, H. D. Lee, M. R. Alves, M. A. Marciano, O. Laskina, Z. Qin, A. V. Tivanski and V. H. Grassian, *Phys. Chem. Chem. Phys.*, 2017, **19**, 21101–21111.
12 S. M. Burrows, E. Gobrogge, L. Fu, K. Link, S. M. Elliott, H. Wang and R. Walker, *Geophys. Res. Lett.*, 2016, **43**, 8306–8313.
13 K. A. Link, C.-Y. Hsieh, A. Tuladhar, Z. Chase, Z. Wang, H. Wang and R. A. Walker, *Chem. Phys.*, 2018, **512**, 104–110.
14 K. A. Link, G. N. Spurzem, A. Tuladhar, Z. Chase, Z. Wang, H. Wang and R. A. Walker, *J. Phys. Chem. A*, 2019, **123**, 5621–5632.
15 K. A. Link, G. N. Spurzem, A. Tuladhar, Z. Chase, Z. Wang, H. Wang and R. A. Walker, *J. Phys. Chem. B*, 2019, **123**, 8931–8938.
16 S. M. Burrows, O. Ogunro, A. A. Frossard, L. M. Russell, P. J. Rasch and S. M. Elliott, *Atmos. Chem. Phys.*, 2014, **14**, 13601–13629.
17 P. K. Quinn, D. B. Collins, V. H. Grassian, K. A. Prather and T. S. Bates, *Chem. Rev.*, 2015, **115**, 4383–4399.
18 R. E. Cochran, O. Laskina, J. V. Trueblood, A. D. Estillore, H. S. Morris, T. Jayarathne, C. M. Sultana, C. Lee, P. Lin, J. Laskin, A. Laskin, J. A. Dowling, Z. Qin, C. D. Cappa, T. H. Bertram, A. V. Tivanski, E. A. Stone, K. A. Prather and V. H. Grassian, *Chem*, 2017, **2**, 655–667.

19 T. H. Bertram, R. E. Cochran, V. H. Grassian and E. A. Stone, *Chem. Soc. Rev.*, 2018, **47**, 2374–2400.
20 C. Leck and E. K. Bigg, *Tellus B*, 2005, **57**, 305–316.
21 M. V. Orellana, P. A. Matrai, C. Leck, C. D. Rauschenberg, A. M. Lee and E. Coz, *Proc. Natl. Acad. Sci. U.S.A.*, 2011, **108**, 13612–13617.
22 C. Leck, Q. Gao, F. Mashayekhy Rad and U. Nilsson, *Atmos. Chem. Phys.*, 2013, **13**, 12573–12588.
23 C. Leck and E. Svensson, *Atmos. Chem. Phys.*, 2015, **15**, 2545–2568.
24 B. G. Pummer, H. Bauer, J. Bernardi, S. Bleicher and H. Grothe, *Atmos. Chem. Phys.*, 2012, **12**, 2541–2550.
25 N. Hiranuma, O. Möhler, K. Yamashita, T. Tajiri, A. Saito, A. Kiselev, N. Hoffmann, C. Hoose, E. Jantsch, T. Koop and M. Murakami, *Nat. Geosci.*, 2015, **8**, 273–277.
26 B. G. Pummer, C. Budke, S. Augustin-Bauditz, D. Niedermeier, L. Felgitsch, C. J. Kampf, R. G. Huber, K. R. Liedl, T. Loerting, T. Moschen, M. Schauperl, M. Tollinger, C. E. Morris, H. Wex, H. Grothe, U. Pöschl, T. Koop and J. Fröhlich-Nowoisky, *Atmos. Chem. Phys.*, 2015, **15**, 4077–4091.
27 T. W. Wilson, L. A. Ladino, P. A. Alpert, M. N. Breckels, I. M. Brooks, J. Browse, S. M. Burrows, K. S. Carslaw, J. A. Huffman, C. Judd, W. P. Kilthau, R. H. Mason, G. McFiggans, L. A. Miller, J. J. Nájera, E. Polishchuk, S. Rae, C. L. Schiller, M. Si, J. V. Temprado, T. F. Whale, J. P. S. Wong, O. Wurl, J. D. Yakobi-Hancock, J. P. D. Abbatt, J. Y. Aller, A. K. Bertram, D. A. Knopf and B. J. Murray, *Nature*, 2015, **525**, 234–238.
28 K. Dreischmeier, C. Budke, L. Wiehemeier, T. Kottke and T. Koop, *Sci. Rep.*, 2017, **7**, 41890.
29 N. Hiranuma, K. Adachi, D. M. Bell, F. Belosi, H. Beydoun, B. Bhaduri, H. Bingemer, C. Budke, H.-C. Clemen, F. Conen, K. M. Cory, J. Curtius, P. J. DeMott, O. Eppers, S. Grawe, S. Hartmann, N. Hoffmann, K. Höhler, E. Jantsch, A. Kiselev, T. Koop, G. Kulkarni, A. Mayer, M. Murakami, B. J. Murray, A. Nicosia, M. D. Petters, M. Piazza, M. Polen, N. Reicher, Y. Rudich, A. Saito, G. Santachiara, T. Schiebel, G. P. Schill, J. Schneider, L. Segev, E. Stopelli, R. C. Sullivan, K. Suski, M. Szakáll, T. Tajiri, H. Taylor, Y. Tobo, R. Ullrich, D. Weber, H. Wex, T. F. Whale, C. L. Whiteside, K. Yamashita, A. Zelenyuk and O. Möhler, *Atmos. Chem. Phys.*, 2019, **19**, 4823–4849.
30 M. J. Wolf, A. Coe, L. A. Dove, M. A. Zawadowicz, K. Dooley, S. J. Biller, Y. Zhang, S. W. Chisholm and D. J. Cziczo, *Environ. Sci. Technol.*, 2019, **53**, 1139–1149.
31 S. Zeppenfeld, M. van Pinxteren, M. Hartmann, A. Bracher, F. Stratmann and H. Herrmann, *Environ. Sci. Technol.*, 2019, **53**, 8747–8756.
32 B. Gantt, N. Meskhidze, M. C. Facchini, M. Rinaldi, D. Ceburnis and C. D. O'Dowd, *Atmos. Chem. Phys.*, 2011, **11**, 8777–8790.
33 L. T. Cravigan, M. D. Mallet, P. Vaattovaara, M. J. Harvey, C. S. Law, R. L. Modini, L. M. Russell, E. Stelcer, D. D. Cohen, G. Olsen, K. Safi, T. J. Burrell and Z. Ristovski, *Atmos. Chem. Phys.*, 2020, **20**, 7955–7977.
34 R. E. Cochran, O. Laskina, T. Jayarathne, A. Laskin, J. Laskin, P. Lin, C. Sultana, C. Lee, K. A. Moore, C. D. Cappa, T. H. Bertram, K. A. Prather, V. H. Grassian and E. A. Stone, *Environ. Sci. Technol.*, 2016, **50**, 2477–2486.
35 F. M. Rad, C. Leck, L. L. Ilag and U. Nilsson, *Rapid Commun. Mass Sp.*, 2018, **32**, 942–950.
36 H. Tervahattu, J. Juhanoja and K. Kupiainen, *J. Geophys. Res.*, 2002, **107**, ACH 18-1.
37 M. Mochida, Y. Kitamori, K. Kawamura, Y. Nojiri and K. Suzuki, *J. Geophys. Res.*, 2002, **107**, 4325.

38 E. M. Adams and H. C. Allen, *Atmosphere*, 2013, **4**, 315–336.
39 E. M. Adams, B. A. Wellen, R. Thiraux, S. K. Reddy, A. S. Vidalis, F. Paesani and H. C. Allen, *Phys. Chem. Chem. Phys.*, 2017, **19**, 10481–10490.
40 B. A. W. Rudd, A. S. Vidalis and H. C. Allen, *Phys. Chem. Chem. Phys.*, 2018, **20**, 16320–16332.
41 M. Shrestha, M. Luo, Y. Li, B. Xiang, W. Xiong and V. H. Grassian, *Chem. Sci.*, 2018, **9**, 5716–5723.
42 P. Degen, M. Paulus, E. Zwar, V. Jakobi, S. Dogan, M. Tolan and H. Rehage, *Surf. Interface Anal.*, 2019, **51**, 1051–1058.
43 F. J. Pavinatto, A. Pavinatto, L. Caseli, dos Santos David S., T. M. Nobre, M. E. D. Zaniquelli and O. N. Oliveira, *Biomacromolecules*, 2007, **8**, 1633–1640.
44 P. Wydro, B. Krajewska and K. Hąc-Wydro, *Biomacromolecules*, 2007, **8**, 2611–2617.
45 B. Krajewska, P. Wydro and A. Jańczyk, *Biomacromolecules*, 2011, **12**, 4144–4152.
46 B. Krajewska, P. Wydro and A. Kyzioł, *Colloid Surface A*, 2013, **434**, 349–358.
47 A. Pavinatto, A. L. Souza, J. A. M. Delezuk, F. J. Pavinatto, S. P. Campana-Filho and O. N. Oliveira, *Colloid Surface B*, 2014, **114**, 53–59.
48 A. Pavinatto, J. A. M. Delezuk, A. L. Souza, F. J. Pavinatto, D. Volpati, P. B. Miranda, S. P. Campana-Filho and O. N. Oliveira Jr., *Colloid Surface B*, 2016, **145**, 201–207.
49 H. Parra-Barraza, M. G. Burboa, M. Sánchez-Vázquez, J. Juárez, F. M. Goycoolea and M. A. Valdez, *Biomacromolecules*, 2005, **6**, 2416–2426.
50 K. de Meijere, G. Brezesinski, O. Zschörnig, K. Arnold and H. Möhwald, *Physica B*, 1998, **248**, 269–273.
51 D. Huster and K. Arnold, *Biophys. J.*, 1998, **75**, 909–916.
52 D. Huster, G. Paasche, U. Dietrich, O. Zschörnig, T. Gutberlet, K. Gawrisch and K. Arnold, *Biophys. J.*, 1999, **77**, 879–887.
53 E. S. Hasenecz, C. P. Kaluarachchi, H. D. Lee, A. V. Tivanski and E. A. Stone, *ACS Earth Space Chem.*, 2019, **3**, 2539–2548.
54 P. a. J. Gorin and J. F. T. Spencer, *Can. J. Chem.*, 1966, **44**, 993–998.
55 A. Linker and R. S. Jones, *J. Biol. Chem.*, 1966, **241**, 3845–3851.
56 A. Haug, B. Larsen, O. Fykse, A. Block-Bolten, J. M. Toguri and H. Flood, *Acta Chem. Scand.*, 1962, **16**, 1908–1918.
57 A. Haug, B. Larsen, O. Smidsrød, O. Smidsrød, G. Eriksson, R. Blinc, S. Paušak, L. Ehrenberg and J. Dumanović, *Acta Chem. Scand.*, 1967, **21**, 691–704.
58 A. Haug, S. Myklestad, B. Larsen, O. Smidsrød, G. Eriksson, R. Blinc, S. Paušak, L. Ehrenberg and J. Dumanović, *Acta Chem. Scand.*, 1967, **21**, 768–778.
59 H. Grasdalen, B. Larsen and O. Smidsrød, *Carbohyd. Res.*, 1979, **68**, 23–31.
60 F. A. Johnson, D. Q. M. Craig and A. D. Mercer, *J. Pharm. Pharmacol.*, 1997, **49**, 639–643.
61 K. Y. Lee and D. J. Mooney, *Prog. Polym. Sci.*, 2012, **37**, 106–126.
62 E. R. Morris, D. A. Rees, D. Thom and J. Boyd, *Carbohyd. Res.*, 1978, **66**, 145–154.
63 Y. Fang, S. Al-Assaf, G. O. Phillips, K. Nishinari, T. Funami, P. A. Williams and L. Li, *J. Phys. Chem. B*, 2007, **111**, 2456–2462.
64 H. Hecht and S. Srebnik, *Biomacromolecules*, 2016, **17**, 2160–2167.
65 R. Kohn, *Pure Appl. Chem.*, 1975, **42**, 371–397.
66 A. Malovíková, M. Rinaudo and M. Milas, *Biopolymers*, 1994, **34**, 1059–1064.
67 I. Donati, A. Cesàro and S. Paoletti, *Biomacromolecules*, 2006, **7**, 281–287.
68 I. Donati, F. Asaro and S. Paoletti, *J. Phys. Chem. B*, 2009, **113**, 12877–12886.

69 F. Topuz, A. Henke, W. Richtering and J. Groll, *Soft Matter*, 2012, **8**, 4877.
70 U. T. D. Huynh, A. Lerbret, F. Neiers, O. Chambin and A. Assifaoui, *J. Phys. Chem. B*, 2016, **120**, 1021–1032.
71 W.-C. Chin, M. V. Orellana and P. Verdugo, *Nature*, 1998, **391**, 568–572.
72 P. Verdugo, A. L. Alldredge, F. Azam, D. L. Kirchman, U. Passow and P. H. Santschi, *Mar. Chem.*, 2004, **92**, 67–85.
73 P. Verdugo, M. V. Orellana, W.-C. Chin, T. W. Petersen, G. van den Eng, R. Benner and J. I. Hedges, *Faraday Discuss.*, 2008, **139**, 393–398.
74 P. Verdugo, *Annu. Rev. Mar. Sci.*, 2012, **4**, 375–400.
75 X. Li, C. Leck, L. Sun, T. Hede, Y. Tu and H. Ågren, *J. Phys. Chem. Lett.*, 2013, **4**, 2637–2642.
76 L. Sun, X. Li, T. Hede, Y. Tu, C. Leck and H. Ågren, *Phys. Chem. Chem. Phys.*, 2014, **16**, 25935–25941.
77 W. Hua, D. Verreault, E. M. Adams, Z. Huang and H. C. Allen, *J. Phys. Chem. C*, 2013, **117**, 19577–19585.
78 W. Humphrey, A. Dalke and K. Schulten, *J. Mol. Graphics*, 1996, **14**, 33–38.
79 L. Martínez, R. Andrade, E. G. Birgin and J. M. Martínez, *J. Comput. Chem.*, 2009, **30**, 2157–2164.
80 S. Jo, T. Kim, V. G. Iyer and W. Im, *J. Comput. Chem.*, 2008, **29**, 1859–1865.
81 S. Jo, K. C. Song, H. Desaire, A. D. MacKerell and W. Im, *J. Comput. Chem.*, 2011, **32**, 3135–3141.
82 S.-J. Park, J. Lee, D. S. Patel, H. Ma, H. S. Lee, S. Jo and W. Im, *Bioinformatics*, 2017, **33**, 3051–3057.
83 S.-J. Park, J. Lee, Y. Qi, N. R. Kern, H. S. Lee, S. Jo, I. Joung, K. Joo, J. Lee and W. Im, *Glycobiology*, 2019, **29**, 320–331.
84 W. L. Jorgensen, J. Chandrasekhar, J. D. Madura, R. W. Impey and M. L. Klein, *J. Chem. Phys.*, 1983, **79**, 926–935.
85 J. Huang and A. D. MacKerell, *J. Comput. Chem.*, 2013, **34**, 2135–2145.
86 K. Han, R. M. Venable, A.-M. Bryant, C. J. Legacy, R. Shen, H. Li, B. Roux, A. Gericke and R. W. Pastor, *J. Phys. Chem. B*, 2018, **122**, 1484–1494.
87 J. Yoo and A. Aksimentiev, *Physical Chemistry Chemical Physics*, 2018, **20**, 8432–8449.
88 E. Duboué-Dijon, M. Javanainen, P. Delcroix, P. Jungwirth and H. Martinez-Seara, *J. Chem. Phys.*, 2020, **153**, 050901.
89 F. Perez and B. E. Granger, *Comput. Sci. Eng.*, 2007, **9**, 21–29.
90 D. R. Roe and T. E. Cheatham, *J. Chem. Theory Comput.*, 2013, **9**, 3084–3095.
91 H. J. C. Berendsen, D. van der Spoel and R. van Drunen, *Comput. Phys. Commun.*, 1995, **91**, 43–56.
92 F. J. Millero, R. Feistel, D. G. Wright and T. J. McDougall, *Deep-Sea Res. Pt. I*, 2008, **55**, 50–72.
93 F. J. Millero, *Chemical oceanography*, Taylor & Francis, Boca Raton, 4th ed., 2013.
94 P. B. Miranda, Q. Du and Y. R. Shen, *Chem. Phys. Lett.*, 1998, **286**, 1–8.
95 J. R. Kanicky and D. O. Shah, *J. Colloid Interf. Sci.*, 2002, **256**, 201–207.
96 D. S. McLean, D. Vercoe, K. R. Stack and D. Richardson, *Appita J.*, 2005, **58**, 362.
97 H. Bu, A.-L. Kjøniksen, A. Elgsaeter and B. Nyström, *Colloid Surface A*, 2006, **278**, 166–174.
98 G. M. Marion, F. J. Millero, M. F. Camões, P. Spitzer, R. Feistel and C.-T. A. Chen, *Mar. Chem.*, 2011, **126**, 89–96.

99 J. K. Denton, P. J. Kelleher, M. A. Johnson, M. D. Baer, S. M. Kathmann, C. J. Mundy, B. A. W. Rudd, H. C. Allen, T. H. Choi and K. D. Jordan, *Proc. Natl. Acad. Sci. U.S.A.*, 2019, **116**, 14874–14880.
100 M. Luo, N. A. Wauer, K. J. Angle, A. C. Dommer, M. Song, C. M. Nowak, R. E. Amaro and V. H. Grassian, *Chem. Sci.*, 2020, **11**, 10647–10656.
101 T. M. Aida, T. Yamagata, M. Watanabe and R. L. Smith, *Carbohyd. Polym.*, 2010, **80**, 296–302.
102 J. Lu, H. Yang, J. Hao, C. Wu, L. Liu, N. Xu, R. J. Linhardt and Z. Zhang, *Carbohyd. Polym.*, 2015, **122**, 180–188.
103 K. A. Carter-Fenk and H. C. Allen, *Atmosphere*, 2018, **9**, 503.
104 H.-J. Butt, K. Graf and M. Kappl, *Physics and chemistry of interfaces*, Wiley-VCH Verlag GmbH & Co. KGaA, Weinheim, Germany, Third, Revised and Enlarged Edition., 2013.
105 C. Y. Tang, Z. Huang and H. C. Allen, *J. Phys. Chem. B*, 2011, **115**, 34–40.
106 P. Balzerowski, K. Meister, J. Versluis and H. J. Bakker, *Phys. Chem. Chem. Phys.*, 2016, **18**, 2481–2487.
107 N. Tanaka, H. Kitano and N. Ise, *Macromolecules*, 1991, **24**, 3017–3019.
108 D. E. Gragson and G. L. Richmond, *J. Phys. Chem. B*, 1998, **102**, 3847–3861.
109 H. C. Allen, N. N. Casillas-Ituarte, M. R. Sierra-Hernández, X. Chen and C. Y. Tang, *Phys. Chem. Chem. Phys.*, 2009, **11**, 5538–5549.
110 E. Le Calvez, D. Blaudez, T. Buffeteau and B. Desbat, *Langmuir*, 2001, **17**, 670–674.
111 S. Kundu and D. Langevin, *Colloid Surface A*, 2008, **325**, 81–85.
112 C. Y. Tang, Z. Huang and H. C. Allen, *J. Phys. Chem. B*, 2010, **114**, 17068–17076.
113 J. F. Neal, W. Zhao, A. J. Grooms, A. H. Flood and H. C. Allen, *J. Phys. Chem. C*, 2018, **122**, 26362–26371.
114 W. Lin, A. J. Clark and F. Paesani, *Langmuir*, 2015, **31**, 2147–2156.
115 G. T. Grant, E. R. Morris, D. A. Rees, P. J. C. Smith and D. Thom, *FEBS Lett.*, 1973, **32**, 195–198.
116 B. T. Stokke, O. Smidsroed, P. Bruheim and G. Skjaak-Braek, *Macromolecules*, 1991, **24**, 4637–4645.
117 B. T. Stokke, K. I. Draget, O. Smidsrød, Y. Yuguchi, H. Urakawa and K. Kajiwara, *Macromolecules*, 2000, **33**, 1853–1863.
118 L. Li, Y. Fang, R. Vreeker, I. Appelqvist and E. Mendes, *Biomacromolecules*, 2007, **8**, 464–468.
119 R. Mendelsohn, J. W. Brauner and A. Gericke, *Annu. Rev. Phys. Chem.*, 1995, **46**, 305–334.
120 K. A. Carter-Fenk, K. Carter-Fenk, M. E. Fiamingo, H. C. Allen and J. M. Herbert, *Chem. Sci.*, 2021, **12**, 8320–8332.